

MODELS OF SYNCHROTRON X-RAYS FROM SHELL SUPERNOVA REMNANTS

STEPHEN P. REYNOLDS

Physics Department, North Carolina State University, P.O. Box 8202, Raleigh, NC 27695-8202; steve_reynolds@ncsu.edu

Received 1997 March 1; accepted 1997 August 29

ABSTRACT

The diffusive shock acceleration process can accelerate particles to a maximum energy depending on the shock speed and age and on any competing loss processes on the particles. The shock waves of young supernova remnants can easily accelerate electrons to energies in excess of 1 TeV, where they can produce X-rays by the synchrotron process. I describe a detailed calculation of the morphology and spectrum of synchrotron X-rays from supernova remnants. Remnants are assumed to be spherical and in the Sedov evolutionary phase, though the results are insensitive to the detailed dynamics. The upstream magnetic field is assumed uniform; downstream it is assumed to be compressed but not additionally turbulently amplified. In all cases, spectra begin to depart from power laws somewhere in the optical to UV range and roll off smoothly through the X-ray band. I show that simple approximations for the electron emissivity are not adequate; a full convolution of the individual electron synchrotron emissivity with a calculated electron distribution at each point in the remnant is required. Models limited by the finite shock age, by synchrotron or inverse Compton losses on electrons, or by escape of electrons above some energy have characteristically different spectral shapes, but within each class, models resemble one another strongly and can be related by simple scalings. The images and spectra depend primarily on the remnant age, the upstream magnetic field strength, and the level of magnetic turbulence near the shock in which the electrons scatter. In addition, images depend on the viewing or aspect angle between the upstream magnetic field and the line of sight. The diffusion coefficient is assumed to be proportional to particle energy (or mean free path proportional to gyroradius), but I investigate the possibility that the proportionality constant becomes much larger above some energy, corresponding to an absence of long-wavelength MHD waves. Models producing similar spectra may differ significantly in morphology, which allows for possible discriminations. I parameterize the model spectra in terms of a slope at 4 keV and a factor by which the X-ray flux density at that energy falls below the extrapolated radio spectrum. Synchrotron radiation may contribute significantly to the X-ray emission of remnants up to several thousand years old.

Subject headings: acceleration of particles — radiation mechanisms: nonthermal — shock waves — supernova remnants — X-rays: ISM

1. INTRODUCTION

By default, the origin of cosmic-ray ions and electrons has been assumed to be supernovae and their remnants, at least up to the “knee” in the cosmic-ray spectrum around 10^{15} eV where a slight steepening takes place (Gaisser 1994). No other objects are both observed to occur with the requisite frequency and energy and observed to produce at least some kind of power-law population of relativistic particles in some energy range (electrons of 1–10 GeV). Similarly, the theory of diffuse shock acceleration (DSA) has been adopted more or less by consensus as the mechanism responsible for generating relativistic particles by individual supernova remnants (SNRs) (see Blandford & Eichler 1987 for an extensive review of shock acceleration theory). The simplest test-particle versions, in which an energetically insignificant population of superthermal particles is magically injected into a plane shock with a step velocity profile, give approximately the correct spectral index [for relativistic particles, $N(E) \propto E^{-s}$, with $s = (r + 2)/(r - 1)$ for a shock compression ratio of r] (Blandford & Eichler 1987). The rough agreement with observed spectral indices of SNRs, along with the sufficient energetics, has been enough to convince most of the community that diffusive shock acceleration in SNR shocks produces the Galactic cosmic rays up to the “knee.”

However, direct evidence for the presence of ions at any energy, or for any particles with energies anywhere near the

required maximum of order 10^{15} eV, is very weak, though recent work has claimed associations between unidentified Galactic-plane EGRET sources and a few supernova remnants (Esposito et al. 1996). Furthermore, simple theoretical considerations seem to indicate that supernova remnants may have trouble producing particles with the highest required energies (Lagage & Cesarsky 1983).

In the standard DSA scheme, particles are assumed to scatter from MHD waves of some kind in the background plasma, either preexisting or generated by the counterstreaming ions themselves (Bell 1978). Analytic and semi-analytic calculations typically rely on a parameterization of the diffusion coefficient, κ , in terms of particle momentum, p (unless they assume it constant): $\kappa \propto p^\beta$, with $\beta = 1$ being a popular choice, amounting to mean free path proportional to particle gyroradius, $\lambda_{\text{mfp}} = \eta r_g$, with η the “gyrofactor.” A given choice of β corresponds, at least in quasi-linear theory, to the spectral index of the MHD waves. This simple parameterization is not totally at odds with hybrid simulation results (Giagalone et al. 1992). Some indirect evidence for the existence of the required waves comes from sharp edges of radio emission in some young SNRs (Achterberg, Blandford, & Reynolds 1994; hereafter ABR), with inferred intensities orders of magnitude greater than that typical of the interstellar medium, which indicates local generation of waves, presumably by the accelerated particles themselves as predicted (Bell 1978). But virtually nothing is known of

the wave spectrum, so β remains essentially a free parameter, as does the proportionality constant, η , which reflects the energy density in waves resonant with particles of the appropriate energy. It is generally presumed that the mean free path can be no less than the gyroradius, so $\eta \geq 1$, with equality implying a level of turbulence such that wave amplitudes are comparable to the static magnetic field strength, $\delta B \sim B$: the Bohm limit.

The most serious concern with DSA in SNRs as a source of cosmic rays probably remains the maximum-energy problem. Lagage & Cesarsky (1983) found that the maximum energy to which particles can be accelerated is limited by the remnant age as long as the shock has not decelerated appreciably. Once it begins the transition to the Sedov self-similar stage, with shock radius $R_s \propto t^{0.4}$, the maximum attainable energy rises more slowly, asymptotically reaching a few times the value it has at the transition to Sedov dynamics. (At late times, energetic particles may be able to diffuse so far ahead of the shock that they escape from the remnant environs altogether, resulting in a slowly dropping maximum energy.) The maximum acceleration rate varies inversely with the diffusion coefficient, so that the highest attainable energies occur at the Bohm limit. However, Jokipii (1987) has pointed out that for large shock obliquity angles, θ_{Bn} , between the upstream magnetic field and the shock normal, more efficient acceleration via the “shock drift” mechanism begins to raise the acceleration rate above the isotropic DSA value. The improvement factor varies roughly as the square of the gyrofactor, so that in very strong turbulence the rates are the same (also to be expected, since in this case the shock is so turbulent that it does not have a well-defined obliquity at all). But the operation of this effect where a SNR shock is nearly perpendicular ($\theta_{Bn} \sim 90^\circ$) might allow SNRs to produce particles approaching the “knee” energy.

Most attention has been given to the problem of accelerating cosmic-ray ions. Electrons have the enormous advantage of being directly observable in SNRs. They suffer additional loss processes affecting the maximum energy to which they can be accelerated, but since cosmic-ray electrons have only been observed directly to about 10^{12} eV (see Reynolds 1992 for a review), there is no conflict with observations even if the maximum energy is well below the “knee”. Rather, the problem is the reverse: accounting for expected loss processes (primarily synchrotron radiation) still predicts that electrons should be accelerated to energies of order 10^{12} eV (1 TeV) or higher, so that SNRs should be sources of nonthermal radiation all the way from radio to X-rays. Refining this prediction is the goal of the present work.

The idea that shock acceleration could produce electrons energetic enough to emit synchrotron X-rays dates at least to Reynolds & Chevalier (1981) in an analysis of early X-ray spectral observations of the historical remnant of the supernova of A. D. 1006 (SN 1006) (Becker et al. 1980; Toor 1980). That work used somewhat naive ideas of shock acceleration, and the X-ray data were also confused. More recently the idea was resurrected by Ammosov et al. (1994), by Reynolds (1995, 1996), and by Reynolds & Hornschemeier (1996), where it was shown that somewhat different sets of detailed assumptions both resulted naturally in the production of kilo-electron volt X-rays. The work by Ammosov et al. used some quite simple assumptions and a value of β of $\frac{1}{2}$ and predicted considerable upstream emis-

sion that is not seen. Reynolds (1996; hereafter, Paper I) incorporated obliquity dependence of the maximum energy using the formalism of Jokipii (1987) and found both spectra and images consistent with X-ray data on SN 1006. It is the goal of this paper to provide a detailed description of the formalism used for these calculations and to exhibit model spectra and images for a wide range of values of relevant parameters, most importantly including remnant age. I shall show that the case of SN 1006 is not completely abnormal: significant nonthermal X-ray components of SNRs should persist for ages up to several thousand years and should be evident in all the historical remnants. However, the unique status of SN 1006 as dominated by nonthermal X-rays is a natural consequence of its age and environment, as will be shown below.

One might imagine that a simple calculation could be done, involving extending the radio power law out to some cutoff photon energy, $h\nu_{\max}$, above which it cuts off exponentially, with $h\nu_{\max}$ related to a simply derived maximum electron energy, E_{\max} . This is unfortunately very far from the case. First, an exponential cutoff in the photon spectrum will occur only for an unreasonable truncated electron distribution; the sharpest plausible cutoff in an electron distribution generated at a shock is likely to be close to exponential, as is predicted explicitly for acceleration limited by a finite time available (Forman & Drury 1983; Drury 1991) or by radiative losses (Webb, Drury, & Biermann 1984). For an exponentially cut off electron distribution, the standard δ -function approximation for the single-electron synchrotron emissivity then predicts a photon spectrum cutting off as $\exp[-(v/v_m)^{1/2}]$. Even this does not turn out to be an adequate approximation; if an exponentially cut off distribution is folded through the complete single-particle synchrotron emissivity, the resulting photon emissivity curves much more broadly than an exponential in v/v_m and somewhat more broadly than the exponential in $(v/v_m)^{1/2}$. Then, since the acceleration time depends on shock obliquity in this model, different parts of the remnant will produce different maximum energies. Finally, since the postshock magnetic field strength will also vary with obliquity, radiative and adiabatic losses downstream will result in a broad spatial variation of the electron distribution. If the shock is decelerating, peak energies attained in the past were different than now, so the integrated spectrum from the remnant is a superposition of various broadly curving spectra in a way impossible to estimate except by explicit calculation, as will be done below.

2. DYNAMICAL ASSUMPTIONS

In the models, the time evolution of the shock is embodied in the electron distribution in the interior. For the calculations below, I shall need the density history and the shock velocity when a given fluid element was shocked. My model remnants are in the Sedov evolutionary phase, and these quantities are readily calculated. However, since, as shall be shown below, the emission is normally dominated from close behind the shock, the detailed dynamics will not strongly affect the predicted spectrum or images. The speed at which a given element was shocked rises to infinity at the remnant center in the Sedov solution, however, so I simply truncate the emission interior to the radius at which that velocity was the presumed ejection velocity of the supernova. (The effects of changing that ejection velocity are described below.) For the remnant ages I

shall consider, that radius contains very little of the remaining mass. In later work, I shall investigate the effects of using different dynamical assumptions, such as the Sedov solution for expansion into a medium with a power-law density profile, or a self-similar driven wave (Chevalier 1982).

Standard numerical values in general are those appropriate to Type Ia supernovae, in particular roughly those of SN 1006: an explosion energy of 10^{51} ergs, an ejection velocity of $u_0 = 10^9$ cm s $^{-1}$, and a (constant) upstream density of $n_0 = 0.1$ cm $^{-3}$ with assumed cosmic abundances (mean molecular weight, μ , is equal to 1.4).

The magnetic field is assumed uniform upstream, with a strength that is a free parameter. It is compressed in the shock with the tangential component rising by a factor of the shock compression ratio, r (normally taken to be 4, in the $\gamma = 5/3$ adiabatic strong-shock limit), so that the immediate postshock magnetic field varies by a factor of 4 with position in the remnant. No further amplification of the magnetic field is assumed; it evolves by flux-freezing behind the shock. The relevant parameter is the shock obliquity, θ_{Bn} , the angle between the shock normal and the external magnetic field.

3. EVOLUTION OF THE ELECTRON DISTRIBUTION

A priori calculations of the spectrum of shock-accelerated electrons to be expected from an evolving SNR shock do not yet exist. The detailed mechanisms and efficiency of electron injection are not well known, and the detailed shock profile will depend as well on the nonlinear feedback between ion injection and acceleration. However, the work of Ellison & Reynolds (1991) demonstrates that above several tens of giga-electron volts, the electron distribution produced by a single steady nonlinear shock approaches the simple power-law form given by test-particle theory. (Note that this does not occur until significantly above the energies responsible for centimeter radio emission, in which curvature of the electron spectrum is still important; Reynolds & Ellison 1992.) The simplest approach, therefore, is to assume that the shock endows each fluid element with a power-law electron distribution, $N(E) = KE^{-s}$ electrons cm $^{-3}$ ergs $^{-1}$, with a normalization, K , that is a free parameter. This normalization might be expected on theoretical grounds to vary with shock velocity, u_{sh} , though there is no unambiguous functional form predicted. I shall calculate spectra primarily for $K = \text{constant}$, though I shall also show a few results for $K \propto u_{\text{sh}}^2$ and $K \propto u_{\text{sh}}$, which show only small differences from the $K = \text{constant}$ case. The numerical value of K at some radius is related to the overall efficiency of electron acceleration, which is not known in general, though it could be deduced from observations if the magnetic field strength in some remnant could be inferred independently.

The nature of the dependence of K on shock velocity can have an important effect on the history of particle acceleration in a remnant. If a roughly constant fraction of thermal electrons entering the shock become accelerated to relativistic energies, we would expect the total number of accelerated electrons in the remnant, N_e , to obey $dN_e/dt \propto R_{\text{sh}}^2 u_{\text{sh}}$, where R_{sh} is the shock radius. In this case, free expansion would imply $dN_e/dt \propto t^2$, that is, electrons injected at earlier times are swamped by those injected later. However, in the Sedov phase, $dN_e/dt \propto t^{-1/5}$, so that the injection rate of cosmic-ray electrons remains roughly constant. I shall

use this reasoning below to justify ignoring the contribution to the electron distribution from electrons injected well before the transition to Sedov dynamics.

3.1. Acceleration Rates and Maximum Energies

The DSA process is expected to continue to energies at which particles somehow escape or lose energy to some process as fast as they gain it. For electrons, three limitations to the maximum energy arise naturally. First, synchrotron or inverse Compton (IC) losses, which vary as E^2 , will eventually limit electron energies. Since the radiation energy density in a SNR is typically dominated by cosmic microwave background (CMB) photons, IC on CMB photons is the only significant source of IC losses (Gaisser, Protheroe, & Stanev 1998). In fact, the CMB energy density is the same as that of a magnetic field of strength $B_{\text{CMB}} = 3.27$ μG , so that whenever the magnetic field strength in the SNR is below that value, IC losses are more important than synchrotron losses in limiting electron energies. Second, the finite age of the remnant may provide a more stringent limit. Third, the electron scattering required for acceleration may become less efficient above some energy (in the limiting case, electrons may simply freely escape above some energy). In the first two of these cases, we expect an exponential cutoff in the electron distribution above some E_{max} set by equating the acceleration time to the shorter of the remnant age or the synchrotron loss time. In fact, Drury's (1991) calculation shows that the actual accelerated-particle distribution function is fit to within 10% by an exponential cutoff with e -folding energy 1.8 times that given by the simple calculation. Detailed calculations for radiative losses (Webb et al. 1984) show that there as well an exponential cutoff is expected.

For the escape case, we shall assume MHD scattering waves are much weaker above some wavelength, λ_{max} , and E_{max} will just be the energy of particles with that gyroradius, roughly. The detailed form of the cutoff in this case would depend on the distribution of waves in direction but is unlikely to be more rapid than exponential. I shall thus assume that for all loss processes, the electron distribution to be found immediately downstream of the shock is a power law, exponentially cut off at the lowest of the three maximum energies because of the three possible limitations.

One might think that a fundamental limit is that for which electrons' gyroradius are comparable to the remnant diameter. However, it can be shown (Lagage & Cesarsky 1983) that this limit is always less stringent than those outlined above. More significant is the possibility that the electron diffusion length, κ/u_{sh} , can become comparable to the shock radius, in which case electrons may diffuse away from the remnant altogether; this limit can be shown to occur only at times late compared to those considered here (i.e., $t \gtrsim 10^4$ yr; Baring et al. 1998).

To calculate acceleration times, we need a model of electron diffusion. I shall assume a mean free path (along the magnetic field) proportional to gyroradius, $\lambda_{\parallel} = \eta r_g$, with η the "gyrofactor." (This quantity, called f in Paper I, has been renamed for consistency with earlier usage such as Jokipii 1987.) In the quasi-linear formalism, η is related to the energy density in resonant waves $(\delta B/B)_{\text{res}}$: $\eta = (\delta B/B)_{\text{res}}^{-2}$, where "resonant" means the wavevector, k , equals $1/r_g$ (e.g., Blandford & Eichler 1987). Thus the assumption of η constant with energy amounts to an assumption about the spectrum of turbulence, unless η is

small, in which case the turbulence is strong and quasi-linear theory is not appropriate. The escape model then corresponds to a sudden rise in η to a much larger value for particles above some energy, so that such particles stream more or less freely away from the remnant. Note that I shall assume η to be constant across the shock.

We then have a diffusion coefficient along the magnetic field:

$$\kappa_{\parallel} \equiv \lambda_{\parallel} v/3 = \eta Ec/3eB, \quad (1)$$

where E is the electron energy, and we have assumed $E \gg m_e c^2$. Across the magnetic field, we shall make the standard assumption (see, e.g., Jokipii 1987) that a particle scatters one gyroradius across field lines for every longitudinal scattering length, so $\kappa_{\perp} = \kappa_{\parallel}/[1 + (\lambda_{\parallel}/r_g)^2] \equiv \kappa_{\parallel}/(1 + \eta^2)$, and the effective diffusion coefficient in the radial direction (along the shock normal) is

$$\kappa = \kappa_{\parallel} \cos^2 \theta_{Bn} + \kappa_{\perp} \sin^2 \theta_{Bn}. \quad (2)$$

So the diffusion coefficient in the upstream direction, κ_1 , is given by

$$\kappa_1 = \frac{\eta c E}{3eB_1} \left(\cos^2 \theta_{Bn1} + \frac{\sin^2 \theta_{Bn1}}{1 + \eta^2} \right). \quad (3)$$

The acceleration time from momentum p_i to p is given by the well-known expression (see, e.g., Forman & Morfill 1979; Drury 1983),

$$\tau_{acc} = \frac{3}{u_1 - u_2} \int_{p_i}^p \left(\frac{\kappa_1}{u_1} + \frac{\kappa_2}{u_2} \right) \frac{dp'}{p'}, \quad (4)$$

where subscripts 1 and 2 indicate upstream and downstream quantities in the shock frame (so $u_1 \equiv u_{sh}$, and $u_2 = u_1/r$ with r the compression ratio), and the shock normal is assumed parallel to the flow direction (normal incidence). For a strictly parallel shock ($\theta_{Bn} = 0$), using equation (3) in the extreme relativistic limit $E = pc$, we have $B_2 = B_1$, so $\kappa_2 = \kappa_1 = \eta c E/3eB_1$, and equation (4) gives

$$\tau_0 = \frac{3}{u_1 - u_2} \frac{\eta c}{3eB_1} \left(\frac{1}{u_1} + \frac{1}{u_2} \right) E, \quad (5)$$

where, since we have assumed $E \gg m_e c^2$, the integral is dominated by the upper limit, and we can ignore the contribution to the acceleration time at much lower energies (including the fact that $E \propto p^2$ below $m_e c^2$). This expression is valid for times short compared to evolutionary timescales on which the shock velocity varies; otherwise, one performs an integral as described below. Since $u_1/u_2 = r$, equation (5) can be rewritten

$$\tau_0 = \frac{\eta c}{eB_1 u_1^2} \frac{r(r+1)}{r-1} E. \quad (6)$$

Let us then define the acceleration time for arbitrary obliquity by $\tau_{acc}(\theta_{Bn}) \equiv \tau_0 R_J(\theta_{Bn})$, giving for R_J ,

$$R_J = \frac{\kappa_1(\theta_{Bn1})/u_1 + \kappa_2(\theta_{Bn2})/u_2}{\kappa_1(0)/u_1 + \kappa_2(0)/u_2}, \quad (7)$$

which is independent of E since all four κ 's are proportional to E ; here the upstream (downstream) angle of the magnetic field with the shock normal is θ_{Bn1} (θ_{Bn2}).

Now if $B_2 \equiv r_B B_1$, we have $\kappa_2(0) = \kappa_1(0)/r_B$, and since the normal component of B is continuous, $B_1 \cos \theta_{Bn1} = B_2 \cos \theta_{Bn2}$. Then

$$R_J = \frac{\cos^2 \theta_{Bn1} + [\sin^2 \theta_{Bn1}/(1 + \eta^2)] + (1/r_B) \cos^2 \theta_{Bn2} + [\sin^2 \theta_{Bn2}/(1 + \eta^2)]}{1/u_1 + 1/u_2}, \quad (8)$$

or

$$R_J \equiv \frac{\cos^2 \theta_1 + \{[\sin^2 \theta_1/(1 + \eta^2)] + r(\cos \theta_2/\cos \theta_1) \times \cos^2 \theta_2 + [\sin^2 \theta_2/(1 + \eta^2)]\}}{1 + r}. \quad (9)$$

This is essentially the expression obtained by Jokipii (1987) (where my R_J is his $1/R_a$ in terms of both θ_1 and θ_2). (I have corrected a minor error: for R_a defined as Jokipii states, the numerator in his eq. [8] should be evaluated for the parallel case, that is, it should be $[1 + r]$ as is the denominator of eq. [9]. See also Ellison, Baring, & Jones 1995.) As Jokipii points out, for large obliquities (and large gyrofactors, η), the effective scattering distance perpendicular to the shock is very small, and shock drift acceleration between scatterings results in a considerable speedup in acceleration ($R_J < 1$). When η is large, R_J can be much less than 1 where the shock is quasi-perpendicular, and the acceleration rate can be much faster than that assuming isotropic diffusion. But as $\eta \rightarrow 1$, that is, for strong turbulence, the distinction between "parallel" and "perpendicular" to the turbulent field becomes lost, and the acceleration rates converge. Furthermore, in order to attain much higher energies than those achievable for intermediate obliquities, particles must accumulate a significant total drift distance (compared to the shock radius) along the shock front, between scatterings.

For a shock with compression ratio r and upstream and downstream magnetic fields B_1 and $B_2 \equiv r_B B_1$, the pitch-angle-averaged time for an electron to reach energy E starting at $E_0 \ll E$ can therefore be written

$$\begin{aligned} \tau_{acc} &= \frac{\eta c}{eB_1} \frac{1}{u_{sh}^2} \left(\frac{r}{r-1} \right) (1+r) E R_J \\ &= 6.25 \times 10^3 \left(\frac{\eta}{B_1} \right) u_8^{-2} F E R_J \text{ s}, \end{aligned} \quad (10)$$

where $u_8 \equiv u_{sh}/(10^8 \text{ cm s}^{-1})$ and

$$F(r) \equiv \left(\frac{r}{r-1} \right) (r+1).$$

Again, this assumes $\tau_{acc} \ll t$, so that we can ignore changes in u_{sh} during the acceleration. For our simple assumption about magnetic field compression, we have

$$r_B = \left(\frac{1 + r^2 \tan^2 \theta_{Bn1}}{1 + \tan^2 \theta_{Bn1}} \right)^{1/2}.$$

Then for $r = 4$, $F = 20/3$ and r_B ranges from 1 at the "poles" ($\theta_{Bn1} = 0$) to 4 at the "equator."

An electron of initial energy E radiating in a uniform magnetic field, B , loses one-half its energy to synchrotron radiation in a time

$$\tau_{1/2} = \frac{637}{\langle B^2 \rangle E} \equiv \frac{637}{B_1^2 E} \text{ G s}, \quad (11)$$

where the last equality, defining G , accounts for an electron spending time in different magnetic fields upstream and downstream of the shock, with the ratio of times given by standard DSA (see, e.g., Ellison, Jones, & Reynolds 1990). We can easily generalize this expression to include inverse Compton losses on the microwave background by defining

$$B_{\text{eff}} \equiv (B^2 + B_{\text{CMB}}^2)^{1/2}, \quad (12)$$

with $B_{\text{CMB}} \equiv 3.27 \mu\text{G}$ the magnetic field strength with energy density equal to that in the CMB.

We can find G by noting that an electron scattering back and forth many times across the shock spends time upstream, t_{up} , and downstream, t_{down} , in the ratio

$$\begin{aligned} \frac{t_{\text{up}}}{t_{\text{down}}} &\cong \frac{\kappa_1}{u_1} \left(\frac{\kappa_2}{u_2} \right)^{-1} \\ &= \frac{r_B}{r} \left\{ \frac{\cos^2 \theta_{\text{Bn1}} + [\sin^2 \theta_{\text{Bn1}}/(1 + \eta^2)]}{\cos^2 \theta_{\text{Bn2}} + [\sin^2 \theta_{\text{Bn2}}/(1 + \eta^2)]} \right\} \equiv \frac{r_B}{r} z, \end{aligned} \quad (13)$$

using equation (3) for the obliquity dependence of the two diffusion coefficients; I assume η to have the same value on both sides of the shock. (The commonly made assumption of $t_{\text{up}} = t_{\text{down}}$, e.g., Draine & McKee 1993, thus requires η varying across the shock.) Then the electron sees an effective mean square magnetic field, $\langle B_{\text{eff}}^2 \rangle$, given by

$$\langle B_{\text{eff}}^2 \rangle = \frac{B_{1\text{eff}}^2 t_{\text{up}} + B_{2\text{eff}}^2 t_{\text{down}}}{t_{\text{up}} + t_{\text{down}}}.$$

Defining $d \equiv B_{\text{CMB}}/B_1$, we can write

$$\langle B_{\text{eff}}^2 \rangle = B_1^2 \left[\frac{(1 + d^2)r_B z + (r_B^2 + d^2)r}{r_B z + r} \right] \equiv \frac{B_1^2}{G},$$

so that

$$G(r, \theta_{\text{Bn}}) = \frac{r_B z + r}{r_B z(1 + d^2) + r(r_B^2 + d^2)},$$

with z defined in equation (13). At the pole, $r = 4$, $r_B = 1$, and $\theta_{\text{Bn1}} = \theta_{\text{Bn2}} = 0$, so $z = 1$ and $G = 1/(1 + d^2)$. At the equator, $r = 4$, $r_B = 4$, and $\theta_{\text{Bn1}} = \theta_{\text{Bn2}} = 90^\circ$, so again $z = 1$ and $G = 2/(17 + 2d^2)$. In the limit of $B_1 \gg B_{\text{CMB}}$ ($d \ll 1$), $G(\text{pole}) = 1$ and $G(\text{equator}) = 2/17$. Equating equations (10) and (11) finally gives us the maximum energy allowed by radiative losses:

$$E_{m1} = 0.32(\eta R_J B_1)^{-1/2} u_8 \left(\frac{G}{F} \right)^{1/2} \text{ ergs}. \quad (14)$$

The effect of IC losses is entirely contained in the factor G .

However, if the remnant age, t , is shorter than the synchrotron lifetime (eq. [11]), the maximum energy attainable will be limited by the finite time available for acceleration. Since the shock velocity will be evolving during the remnant lifetime, we must integrate the differential form of equation (10):

$$dE = AR_J^{-1} u_{\text{sh}}^2 d\tau \quad (15)$$

with

$$A \equiv \frac{r-1}{r(r+1)} \frac{eB_1}{\eta c} \equiv \frac{eB_1}{\eta c F}.$$

Then if the Sedov phase begins at a transition time, t_{tr} , the maximum energy attainable in time $t > t_{\text{tr}}$ is

$$E_{m2} = E_m(t_{\text{tr}}) + \int_{t_{\text{tr}}}^t AR_J^{-1} u_{\text{sh}}^2 dt, \quad (16)$$

where calculating $E_m(t_{\text{tr}})$ requires knowing the complete velocity history of the shock, as well as any time dependence of electron injection. As argued above, the rate at which the shock sweeps over material varies as $R_{\text{sh}}^2 u_{\text{sh}}$, which rises rapidly in any quasi-free expansion phase, strongly diluting the effect on the eventual integrated spectrum of electrons run over at early times when the shock was small. Thus at t_{tr} , the highest energy electrons will be those that were injected in much smaller numbers near $t = 0$, and their contribution will be greatly diluted by those injected more recently, except at the very highest energies that the latter electrons have not had time to reach. Well after t_{tr} , the domain considered in this paper, we have Sedov dynamics so $R_{\text{sh}}^2 u_{\text{sh}} \propto t^{-1/5}$, roughly constant. Thus the contribution to the total spectrum of the electrons injected before t_{tr} should be small, and I shall neglect it. I therefore set $E_m(t_{\text{tr}}) = 0$ in equation (16). Sedov dynamics give $u_{\text{sh}} = 0.46(E/\rho)^{1/5} t^{-3/5}$ and allow us to define t_{tr} in terms of the time at which the Sedov expansion velocity would have been the presumed ejection velocity of a Type Ia supernova, $u_0 = 10^9 \text{ cm s}^{-1}$: $t_{\text{tr}} = 4.45 \times 10^{24} u_0^{-5/3} k^{1/3}$ with $k \equiv E_{51}/[(n_0/(0.1 \text{ cm}^{-3}))(\mu/1.4)]$ and E_{51} the explosion energy in units of 10^{51} ergs. For standard values, $k = 1$ and $t_{\text{tr}} = 141$ yr. Thus we obtain

$$\begin{aligned} E_{m2}(t) &= 5AR_J^{-1} u_0^2 t_{\text{tr}} \left[1 - \left(\frac{t}{t_{\text{tr}}} \right)^{-0.2} \right] \\ &\equiv 5E_{m0} \left[1 - \left(\frac{t}{t_{\text{tr}}} \right)^{-0.2} \right], \end{aligned} \quad (17)$$

where

$$E_{m0} \equiv AR_J^{-1} u_0^2 t_{\text{tr}} = 71.2 k^{1/3} B_1 \mu_{\text{G}} u_9 (FR_J \eta)^{-1} \text{ ergs}, \quad (18)$$

where $u_9 \equiv u_0/(10^9 \text{ cm s}^{-1})$. Equation (17) shows that after the transition to Sedov evolution, the maximum energy from finite-time limitations continues to rise slowly, asymptotically approaching $5E_{m0}$. For numerical calculations, equation (17) is used, after multiplying by 1.8 (Drury 1991); for estimates comparing maximum energies, equation (18) will be used as a typical age-limited maximum energy, actually the maximum energy achieved at a time $t = 3.05 t_{\text{tr}}$. Since the calculations shown here begin at 300 years $> 2 t_{\text{tr}}$ and extend only to a time of 10^4 years $\sim 70 t_{\text{tr}}$, equation (18) gives the right age-limited maximum energy to within a factor of less than 3 and is within 60% at the age of SN 1006.

Finally, if upstream MHD waves have much lower amplitudes above some wavelength, λ_{max} , electrons above E_{m3} will be unable to scatter from them, with E_{m3} given by the resonance condition

$$k \cdot v - \Omega = 0,$$

with Ω the gyrofrequency eBc/E and $k = 2\pi/\lambda_{\text{max}}$. Thus $E = \lambda_{\text{max}} eB/2\pi \cos \psi$ or, averaging over pitch angles ψ ,

$$E_{m3} = \lambda_{\text{max}} eB_1/4, \quad (19)$$

since escape only occurs upstream.

These maximum energies evolve with time. For the Sedov

relation $u_1 \propto t^{-3/5}$, $E_{m1} \propto t^{-3/5}$ (if $\tau_{1/2}$ is considerably less than the remnant age, t), and E_{m2} rises slowly as described above. At early times, the remnant age always limits the maximum energy, but eventually it will be limited by losses.

Several minor errors, in F and G and elsewhere in Paper I, which were corrected above, cause these results to differ slightly (by less than a factor of 2) from those shown there. The most significant change made here involves including the effect of CMB IC in limiting maximum electron energies for low upstream magnetic field strengths. Escape models (including that of Paper I) are unaffected by these various corrections.

3.2. Postshock Evolution of the Distribution Function

Once a particle distribution has been produced at the shock, it will evolve downstream because of further radiative losses and adiabatic expansion losses. I shall approximate the diffusion of electrons downstream as much less effective than upstream, so that electrons remain essentially confined to the fluid element in which they were produced. Then their adiabatic expansion losses are just given by the expansion of that fluid element. Let the downstream density (normalized to its immediate postshock value) be $\rho(r)/\rho_2 \equiv \alpha(r)$. In addition, tracking synchrotron losses will require following the postshock evolution of the magnetic field. Here I shall assume that turbulent amplification processes are negligible, so that the field is simply compressed at the shock and evolves purely by flux-freezing thereafter.

I shall assume that the postshock magnetic field is highly disordered, as indicated for young SNRs by radio polarization observations (see Reynolds & Gilmore 1993 and references therein). Thereafter, the radial and tangential components of the field will evolve differently (Duin & Strom 1975; Reynolds & Chevalier 1981). Let the radial and tangential components of the immediate postshock field be B_{2r} and B_{2t} , respectively. Then if a fluid element currently at radius r was shocked at r_i , we have

$$B_r = B_{2r} \left(\frac{r_i^2}{r^2} \right), \quad B_t = B_{2t} \alpha(r) \left(\frac{r}{r_i} \right), \quad (20)$$

so that in the absence of turbulent amplification, the interior field strength obeys

$$B^2(r) = B_{2r}^2 \left(\frac{r_i^4}{r^4} \right) + 2B_{2t}^2 \alpha^2 \left(\frac{r^2}{r_i^2} \right). \quad (21)$$

Plots of $B_r(r)$, $B_t(r)$, and $B(r)$ are shown in Figure 1. This assumption is slightly different from that used in a preliminary report on this work (Reynolds 1995) where the magnetic energy density was taken to evolve as the density: $B^2 \propto \alpha$. The ultimate differences in electron distributions between that case and the current one are less than 15% at any radius.

An individual electron loses energy both to radiative losses (synchrotron and inverse Compton) and to adiabatic expansion losses. The first effect is given by

$$-\dot{E}_{\text{rad}} = \frac{4}{3} \sigma_T c \left(\frac{E}{m_e c^2} \right)^2 \left(\frac{B_{\text{eff}}^2}{8\pi} \right),$$

where we have averaged over pitch angles and taken the electron velocity, v , to be $\approx c$. Here σ_T is the Thomson cross section. For adiabatic losses, again assuming extreme relativistic electrons, the adiabatic index is $4/3$, so the relativistic energy density obeys $u_e \propto V^{-4/3}$, where V is the

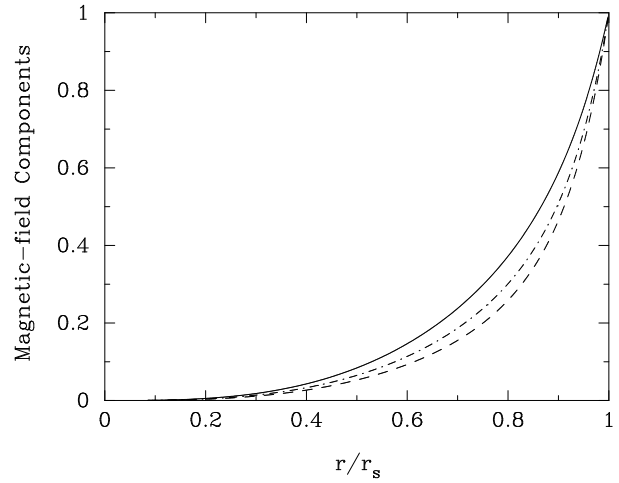


FIG. 1.—Magnetic field evolution behind the shock. B_r (solid line), B_t (dashed line), and B_{tot} (dot-dashed line) are plotted.

volume of the confining fluid element. Then an individual electron's energy $E \propto V^{-1/3}$, or

$$-\dot{E}_{\text{ad}} = \frac{1}{3} \frac{E}{V} \frac{dV}{dt} = -\frac{E}{3\alpha} \frac{d\alpha}{dt}.$$

Defining

$$a \equiv \frac{1}{6\pi} \frac{\sigma_T c}{(m_e c^2)^2} \equiv 1.57 \times 10^{-3} \text{ (cgs)},$$

we can write

$$-\frac{dE}{dt} + \frac{E}{3\alpha} \frac{d\alpha}{dt} = aB_{\text{eff}}^2 E^2. \quad (22)$$

In terms of $w \equiv E/\alpha^{1/3}$, this simplifies to

$$\frac{dw}{dt} = aB_{\text{eff}}^2 E w,$$

giving, in terms of the initial electron energy, E_0 , produced at time t_i ,

$$\frac{1}{E_0} - \frac{\alpha^{1/3}(r)}{E(r)} = \int_{t_i}^t aB_{\text{eff}}^2 \alpha^{1/3} dt'. \quad (23)$$

For prescribed dynamics and magnetic field evolution, the integral can be performed numerically and tabulated. We evolve the electron distribution as follows. At the shock we assume

$$N(E_0) = KE_0^{-s} \exp \left(-\frac{E_0}{E_m} \right),$$

while downstream we must have

$$N(E) = N(E_0) \frac{dE_0}{dE},$$

with $E(E_0)$ given by equation (23):

$$E/E_0 = \alpha^{1/3} \left(1 + E_0 \int_{t_i}^t aB_{\text{eff}}^2 \alpha^{1/3} dt' \right)^{-1}, \quad (24)$$

from which

$$\frac{dE}{dE_0} = \frac{E^2}{E_0^2} \frac{1}{\alpha^{1/3}}$$

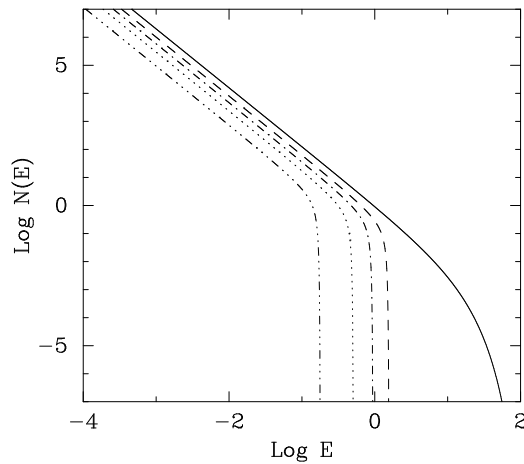


FIG. 2a

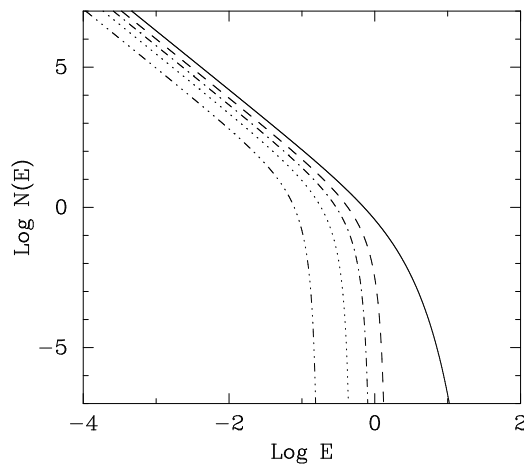


FIG. 2b

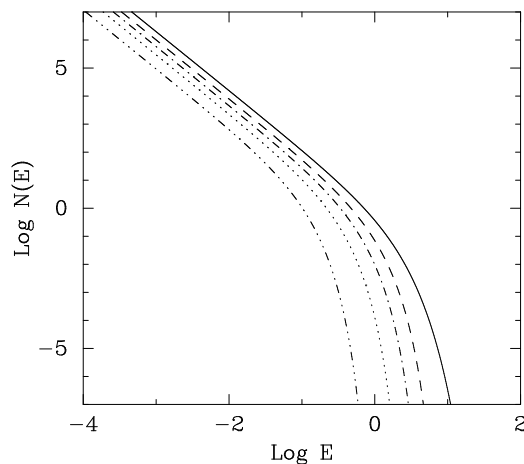


FIG. 2c

FIG. 2.—Electron energy distributions within the remnant. In each figure, the solid line is the distribution at the shock, and the dashed, dot-dashed, dotted, and triple-dot-dashed lines are the distributions at 0.8, 0.6, 0.4, and 0.2 of the shock radius, respectively. Radiative losses become relatively less severe moving from (a) to (c). (a) $E_f = 1$ erg, $E_m = 10$ ergs. (b) $E_f = 1$ erg, $E_m = 1$ erg. (c) $E_f = 10$ ergs, $E_m = 1$ erg.

and

$$N(E) = K[E_0(E)]^{-s} \alpha^{1/3} \left[\frac{E_0(E)}{E} \right]^2 \exp \left[-\frac{E_0(E)}{E_m} \right]. \quad (25)$$

Notice that if we define a dimensionless time variable, $\tau \equiv t'/t$, we can rewrite equation (24) as

$$E/E_0 = \alpha^{1/3} \left[1 + \frac{E_0}{E_f} \int_{\tau_i}^1 \frac{B_{\text{eff}}^2(r)}{B_{2\text{eff}}^2} \alpha^{1/3} d\tau \right]^{-1}, \quad (26)$$

where the dimensional quantities in the integral have been collected into a fiducial energy

$$E_f \equiv a B_{2\text{eff}}^2 t \quad (27)$$

which is the energy an initially infinitely energetic electron would have after radiating for a time t in a constant magnetic field of strength $B_{2\text{eff}}$.

Figure 2 shows the distribution $N(E/E_f)$ at several positions inside the remnant, for $E_m/E_f = 10, 1$, and 0.1 . For large values of this ratio, radiative losses are important, mainly above the adiabatically shifted break in the spectrum [i.e., $E_m(r)$]. For $E_m < E_f$, losses are primarily adiabatic at all energies.

4. UPSTREAM BEHAVIOR OF THE ELECTRON DISTRIBUTION

In the DSA process, particles scatter ahead of the shock, eventually reversing themselves and recrossing the shock for further acceleration. When the mean free path increases with energy, as here, the typical diffusion distance ahead of the shock, $r_D \equiv \kappa(E)/u_{\text{sh}}$, will increase with energy as well. For typical SNR parameters, this distance can be of order arcseconds for radio-emitting electrons (ABR; Reynolds 1994), and for X-rays it could be a significant fraction of the remnant diameter.

If electron energies are limited by radiative losses, the ions presumably also accelerated in the shock can continue to much higher energies, since in SNRs they are never significantly affected by synchrotron losses [for protons, $E_{m1} \propto (m_p/m_e)^2$, a far higher energy than SNRs will ever have time to produce, i.e., for protons $E_{m2} \ll E_{m1}$ always]. In this case the ions would be expected to generate MHD turbulence in which the electrons scatter. For either of the other two loss processes, the preshock electron and ion distributions should be similar. In the absence of strong preexisting turbulence, the cosmic rays themselves will generate waves.

ABR showed that for electrons producing radio synchrotron emission, mean free paths appropriate for typical interstellar levels of magnetic turbulence were far too long to explain four sharp-rimmed supernova remnants and that values of $(\delta B/B)_{\text{res}}$ of several percent or greater were required. The obvious source of this excess turbulence is the counterstreaming cosmic rays themselves (Bell 1978; Blandford & Eichler 1987). Bell (1978) showed that for discontinuous (test-particle) shocks, the preshock particle distribution in the presence of self-generated waves depends on preshock distance, z , by

$$N(E, z) = \frac{N(E, 0)}{1 + z/z_0}, \quad (28)$$

where the scale length, z_0 , is roughly given by

$$z_0 \cong \frac{\kappa(E)}{u_{\text{sh}}} \frac{N(E, 0)}{N(E, z)} \quad (29)$$

(Blandford & Eichler 1987). The relevant wavelength scales for the corresponding turbulence are comparable to the electron gyroradii, or 10^{11} – 10^{12} cm. At the much longer

length scales appropriate for scattering X-ray emitting electrons ($\sim 10^{17}$ cm and greater), little is known about the state of interstellar turbulence. In the absence of other information, I shall assume that the turbulence responsible for scattering these energetic electrons is spatially uniform, so that the electron distribution is given rather by an exponential:

$$N(E, z) = N(E, 0) \exp\left(-\frac{z}{r_D}\right), \quad (30)$$

with r_D constant (see, e.g., Blandford & Eichler 1987). This choice is also implicit in the earlier discussion in which the upstream diffusion coefficient, κ_1 , is assumed uniform. A Bell distribution requires a diffusion coefficient increasing ahead of the shock (or a value of η that increases as one moves ahead of the shock) and will thus require alterations in the expressions for acceleration times above, increasing them somewhat as particles with higher energies sample larger average diffusion coefficients when ahead of the shock. In any case, emission ahead of the shock always represents a small fraction of the total flux from the remnant. However, the detailed form of the preshock "halo" will also differ for a Bell distribution. If such halos are discovered, a more careful look at this issue will be in order. In any case, the exponential distribution will produce the minimum halo, so these results can be regarded as lower limits.

Since electrons in nonescape models are confined to within 10% or 20% of the remnant, the shock sphericity can be adequately accounted for by adding a $1/r^2$ dropoff in the electron distribution ahead of the shock. In the absence of escape, I ignore cross field diffusion upstream, since gyroradii are always small compared to the remnant diameter. However, in escape models a more careful treatment is necessary for the escaping particles, those with $r_g > r_g(\text{max})$. These particles are still subject to diffusion, just with a much longer mean free path ($\eta = 100$ in numerical work). Thus these particles will diffuse away along exterior field lines, with an exponentially dropping distribution (in space) along the direction of field lines, while spreading perpendicular to field lines with a perpendicular diffusion coefficient amounting to an effective $\eta_\perp = 1$.

5. SYNCHROTRON EMISSIVITY AND CALCULATIONS OF IMAGES AND SPECTRA

We now have prescriptions for the electron energy distribution at any point inside or outside the remnant. These will be numerically convolved with the single-electron emissivity (from values tabulated in Pacholczyk 1970) to obtain the volume emissivity at each point. It has been pointed out above that the common δ -function approximation of considering each electron to emit all its energy at its characteristic frequency, $\nu_c = 1.82 \times 10^{18} E^2 B$, would predict, for an electron spectrum cutting off as $\exp(-E/E_m)$, a photon spectrum cutting off as $\exp[-(\nu/\nu_m)^{1/2}]$, which differs significantly from the full calculation. To demonstrate this, Figure 3 shows the synchrotron emissivity from a power-law distribution with an exponential cutoff, i.e., $N(E) = KE^{-s} \exp(-E/E_m)$. For comparison, the corresponding power-law photon distribution cut off exponentially, that is, $j_\nu \propto \nu^\alpha \exp[-\nu/\nu_c(E_m)]$ with $\alpha = (1-s)/2$, is also shown, along with the δ -function emissivity result. The former corresponds to the emissivity from a truncated elec-

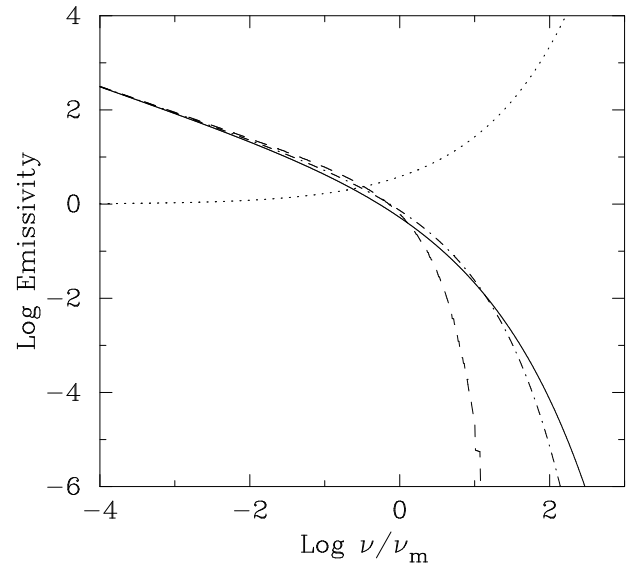


FIG. 3.—Synchrotron emissivity of an electron distribution with cutoff. Exponentially cutoff electron distribution, convolved with the full single-particle synchrotron emissivity (solid line); truncated electron distribution (dashed line), exponentially cut off electron distribution, with the δ -function approximation for the single-particle emissivity (dot-dashed line); and decrement factor (ratio of the extrapolation from low frequencies of a straight power law to the solid line) (dotted line).

tron distribution at E_m , for which emission above $\nu_c(E_m)$ is dominated by the electrons with $E = E_m$, which contribute an emissivity $j_\nu \propto \exp[-\nu/\nu_c(E_m)]$. Figure 3 also shows the ratio by which the calculated emissivity falls below the extrapolation of the straight power law. At frequencies 10 times the frequency corresponding to E_m (i.e., the peak frequency emitted by an electron of energy E_m , $\nu_m = 1.82 \times 10^{18} E_m^2 B$ Hz), the exponentially cut off photon distribution is, of course, smaller by a factor of 22,000, while the calculated distribution has dropped by a factor of less than 30. This slow dropoff means that significant X-rays can be produced far beyond the frequencies corresponding to the first deviation of the electron spectrum from a straight power law.

Images are calculated by integrating the emissivity, numerically calculated as described above, at each point along each line of sight in a raster scan. The magnetic field inside the remnant is presumed sufficiently disordered that a constant average value can be used for the angle between the line of sight and the magnetic field at each point. (The value can be taken to be 60° ; its value is swallowed in the overall normalization as long as it is constant.) However, outside the remnant shock wave, the exterior emission is calculated assuming perfectly straight magnetic field lines. Images are calculated for various values of the aspect angle, ϕ , between the line of sight and the external magnetic field, so for ϕ near 0, the halo emission is strongly suppressed.

A spectrum is generated by calculating a sequence of images, typically two per decade in frequency above 10^{13} Hz or so, and integrating over each to obtain a total flux. For spectra, images are generally only 48×48 , in a box whose side is equal to three remnant radii, while the images shown below are calculated at much higher resolution (192×192). The lower resolution affects the integrated flux by less than 30%. Since the source is always extremely optically thin and the total flux is dominated by interior emission, the spectrum is essentially independent of aspect, to

the same degree of accuracy (though the small contribution of the halo does vary strongly with aspect). Therefore, spectra are calculated only for $\phi = 90^\circ$.

6. RESULTS

Images and spectra calculated for various sets of parameters are shown below. All spectra simply steepen gradually from the low-frequency power law. A simple quantitative description is given in Table 1, which quotes R_{18} , the factor by which the spectrum has dropped below the low-frequency extrapolation at a frequency of 10^{18} Hz (~ 4 keV), and it also gives the slope at that frequency, α_{18} .

(Actually, α_{18} is the average slope between $\nu = 10^{17.5}$ and 10^{18} Hz.) In that frequency range, for typical models the slope steepens by several tenths over a bandpass of a factor of 10, so a broad-spectrum X-ray detector should be able to detect the curvature. The discussion is partitioned as follows. The bulk of the results are for a “standard” model in which the magnetic field is compressed only, the electron distribution spectral index, s , equals 2.1 (the observed value for SN 1006; Green 1991), the normalization of the electron distribution, K , is constant, and the interior emission is cut off inside the radius where the shock velocity would have exceeded $10,000 \text{ km s}^{-1}$ (i.e., $u_8 = 10$). For these standard

TABLE 1
MODEL RESULTS FOR R_{18} AND α_{18}

η	B (G)	Other	Age (yr)	$\log R_{18}$	α_{18}
1	3×10^{-7}	...	990	3.73	-3.0
	6×10^{-7}	...	300	3.32	-2.7
	6×10^{-7}	...	990	1.80	-1.9
	6×10^{-7}	$K \propto u$	990	1.91	-1.9
	6×10^{-7}	$K \propto u^2$	990	2.05	-1.9
	6×10^{-7}	...	3000	1.54	-1.8
	6×10^{-7}	...	10000	2.65	-2.5
	6×10^{-7}	$u_0 = 2 \times 10^4 \text{ km s}^{-1}$	990	1.08	-1.4
	1×10^{-6}	$\lambda_{\text{max}} = 10^{17} \text{ cm}$	990	5.65	-4.2
	1×10^{-6}	$\lambda_{\text{max}} = 10^{18} \text{ cm}$	990	1.28	-1.4
	1×10^{-6}	...	990	0.99	-1.3
	1×10^{-6}	...	10000	2.09	-2.2
	1×10^{-6}	$u_0 = 2 \times 10^4 \text{ km s}^{-1}$	990	0.62	-1.1
	3×10^{-6}	...	990	0.56	-1.0
	3×10^{-6}	...	10000	1.89	-1.9
	1×10^{-5}	...	990	1.04	-1.3
	1×10^{-5}	...	10000	2.40	-1.8
	3×10^{-5}	...	990	1.62	-1.3
	3×10^{-5}	...	10000	2.66	-1.5
3	3×10^{-7}	...	990	2.99	-2.4
	3×10^{-7}	$u_0 = 2 \times 10^4 \text{ km s}^{-1}$	990	2.02	-1.9
	1×10^{-6}	...	990	0.88	-1.2
	3×10^{-6}	...	990	0.46	-0.93
	1×10^{-5}	...	990	0.96	-1.2
10	3×10^{-5}	...	990	1.56	-1.2
	3×10^{-7}	...	990	2.04	-1.6
	6×10^{-7}	...	990	1.22	-1.2
	6×10^{-7}	...	10000	2.23	-1.9
	1×10^{-6}	...	990	0.87	-1.0
	1×10^{-6}	...	10000	1.81	-1.8
	3×10^{-6}	...	300	0.66	-0.89
	3×10^{-6}	$\lambda_{\text{max}} = 10^{16} \text{ cm}$	990	8.69	-6.1
	3×10^{-6}	$\lambda_{\text{max}} = 10^{17} \text{ cm}$	990	1.87	-1.9
	3×10^{-6}	$\lambda_{\text{max}} = 10^{18} \text{ cm}$	990	0.37	-0.87
	3×10^{-6}	...	990	0.52	-0.97
	3×10^{-6}	$K \propto u$	990	0.55	-0.95
	3×10^{-6}	$K \propto u^2$	990	0.65	-0.97
	3×10^{-6}	...	10000	1.64	-1.7
	3×10^{-6}	$u_0 = 2 \times 10^4 \text{ km s}^{-1}$	990	0.40	-0.94
	1×10^{-5}	...	300	0.36	-0.80
	1×10^{-5}	...	990	0.89	-1.2
	1×10^{-5}	...	10000	2.07	-1.6
	3×10^{-5}	...	990	1.49	-1.4
	3×10^{-5}	...	10000	2.24	-1.3
50	3×10^{-7}	...	990	1.65	-1.2
	6×10^{-7}	...	990	1.30	-1.0
	1×10^{-6}	...	990	1.08	-0.94
	3×10^{-6}	...	990	0.80	-1.0
	1×10^{-5}	...	990	1.00	-1.3
	3×10^{-5}	...	990	1.58	-1.2

NOTE.—Ellipsis dots in the “Other” column indicate a model with standard parameters: no escape ($\lambda_{\text{max}} = 10^{20} \text{ cm}$), $K = \text{constant}$, and $u_0 = 10^4 \text{ km s}^{-1}$. At most one of these assumptions is altered for any model, in which case the altered value appears in the “Other” column.

assumptions, I shall first describe characteristics of models limited by each of the three mechanisms for E_m (eqs. [14], [17], and [19]), followed by a discussion of dependence on upstream magnetic field strength, B_1 , gyrofactor, η , escape wavelength, λ_{\max} , and age, t . Thereafter, I shall illustrate in a few cases the effects of relaxing the “standard” assumptions: examining different values of s and maximum allowed u_{sh} and considering $K \propto u_{\text{sh}}$ and $K \propto u_{\text{sh}}^2$.

In the absence of escape, models will always become radiative-loss dominated after a sufficiently long time. We can find that time from equations (14) and (18):

$$\frac{E_{m0}}{E_{m1}} = 0.223 B_{\mu\text{G}}^{3/2} (FG\eta R_J)^{-1/2} k^{1/3} u_8^{-1}, \quad (31)$$

with the time dependence of the ratio appearing through $u_8(t)$. Inserting the appropriate Sedov expression, we find that the ratio is unity at

$$t_{\text{eq}} = 1.1 \times 10^4 B_{\mu\text{G}}^{-5/2} (FG\eta R_J)^{5/6} k^{-2/9} \text{ yr}, \quad (32)$$

a surprisingly long time. This expression is sensitive to parameters. For an upstream density $n_0 = 1 \text{ cm}^{-3}$ ($\Rightarrow k = 10$), an upstream magnetic field strength of $3 \mu\text{G}$, $\eta = 1$, and values of F and G appropriate to near $\theta_{\text{Bn}} = 90^\circ$ where the fastest acceleration takes place (so $FG \sim 1$), we have $t_{\text{eq}} \sim 1000$ years. Since the maximum energies vary with position on the shock face, different portions of the shock will be age or loss limited. We first consider models young enough that they are age-limited everywhere.

6.1. Age-limited models

In this case, interior electron distributions all resemble Figure 2c: that is, the electron distribution is *never* affected by radiative losses, either in being produced at the shock or in subsequent evolution. A typical spectrum is shown in Figure 4, which also includes the (frequency-dependent) spectral index; images at several frequencies for $\phi = 90^\circ$, 60° , and 30° appear in Figure 5. The value of R_{18} , the drop below the extrapolation at 10^{18} Hz ($\sim 4 \text{ keV}$), is about 63, and the slope at that frequency, α_{18} , is approximately -1.9 . This is the “low magnetic field” model for SN 1006 of Paper I: $B_1 = 6 \times 10^{-7} \text{ G}$, $\eta = 1$, and the age ($t = 990$ years) and radius ($r_s = 7.8 \text{ pc}$) appropriate for SN 1006, so $u_8 = 3.1$.

The value of E_{m2} given by equation (17) for these parameters (including Drury’s factor of 1.8) is 337 ergs (211 TeV) at the remnant equator; electrons of that energy, radiating in the equatorial postshock field of $4B_1$, emit their peak power at $\nu_m = 5 \times 10^{17} \text{ Hz}$. At that frequency, the spectrum has dropped about a factor of 20 below the extrapolation of the low-frequency power law. The spectral index is about -1.6 at that frequency. So the great inhomogeneity in the remnant, coupled with the broadening effect shown in Figure 3, allows the spectrum to curve gradually and to contain significant power at energies far above ν_m .

6.2. Loss-limited models

Here the parameters are chosen so that at $\theta_{\text{Bn}} = 90^\circ$, we have $E_{m1} < E_{m2}$ by a comfortable margin. Now from equation (31), recalling that R_J ranges from 1 at $\theta_{\text{Bn}1} = 0$ to $2(1 + \eta^2)^{-1}(1 + r)^{-1}$ at $\theta_{\text{Bn}1} = 90^\circ$ and that G rises toward the equator as well, we see that E_{m2}/E_{m1} is always larger at the equator than at the poles—that is, a model is more

likely to be loss-limited at the equator. Since most of the flux at the highest energies comes from near the equator (all three expressions for E_m are largest there), if E_{m1} is considerably less than E_{m2} there, the model will be loss-limited. In the interior, there may be a radius at which (i.e., in the past) the age limitation was more stringent, but that radius may fall interior to that at which we set the emissivity to zero (because u_{sh} there was $10,000 \text{ km s}^{-1}$). Even if that is not the case, in most models the emission is dominated by radii closest to the shock, so the integrated spectrum will be loss-limited.

Figure 6 shows the spectrum and spectral index of a loss-limited model, with a rather large upstream magnetic field: $B_1 = 10^{-5} \text{ G}$ and $\eta = 10$. The age and radius are the same as before. The spectrum has dropped only by a factor of 5 at 10^{18} Hz , and the slope has steepened merely to $\alpha_{18} = -1.1$. The amount of steepening is very much less than for the age-limited model. Equation (14) gives a maximum energy of 290 ergs at the equator (only 37 ergs at the pole); 290 erg electrons in the equatorial postshock field of $4 \times 10^{-5} \text{ G}$ radiate their peak power at $\nu_{m1} = 6 \times 10^{18} \text{ Hz}$, by which the spectrum has dropped a factor ~ 30 below the radio extrapolation. (Thus for these parameters, the equatorial maximum value of E_{m1} does not characterize well the integrated spectrum. This issue is discussed further in § 6.5 below.) The images at the same frequencies, shown in Figure 7, are markedly different.

6.3. Escape-limited models

We describe escape models in terms of a maximum wavelength of MHD waves, λ_{\max} , with $E_{m3} \propto \lambda_{\max} B_1$ by equation (19). So E_{m3} is essentially a free parameter. Figures 8 and 9 show spectra and images for the escape model of Paper I: $B_1 = 3 \mu\text{G}$, $\lambda_{\max} = 1 \times 10^{17} \text{ cm}$, $\eta = 10$, and r_s and t are as above. Fitting the data for SN 1006 required $E_{m3} = 36 \text{ ergs}$; at that energy, electrons radiate primarily at $\nu_{m3} = 2.8 \times 10^{16} \text{ Hz}$, where the spectrum has dropped by a factor of 2.5 from the low-frequency extrapolation. The spectrum is very similar in shape to that of the low magnetic field model above: $R_{18} = 74$ and $\alpha_{18} = -1.9$.

6.4. Magnetic Field Dependence

Varying the upstream magnetic field strength, B_1 , in models while keeping other parameters fixed can change the model from age-limited to loss-limited, with the concomitant change in shape of the spectrum pointed out above. From equation (31), we find the magnetic field strength at which $E_{m1} = E_{m2} \sim E_{m0}$ to be

$$B_1(\text{eq}) = 2.64 (FG\eta R_J)^{1/3} (t/1000 \text{ yr})^{-2/5} k - 4/45 \mu\text{G}. \quad (33)$$

Since G depends somewhat on B_1 through $d \equiv B_{\text{CMB}}/B_1$, this equation is actually an implicit equation for B_1 , but the dependence of the right-hand side on B_1 is quite weak. Now in the age-limited regime, E_{m2} rises with B_1 , while in the loss-limited regime, E_{m1} falls as $B_1^{-1/2}$. So at $B_1 = B_1(\text{eq})$, we expect the strongest X-rays at a given frequency. The fortuitous near coincidence of $B_1(\text{eq})$ with a typical interstellar magnetic field strength, for SN 1006 parameters, may be one reason that the synchrotron X-ray component in that object is so much more apparent than for the other historical shell remnants.

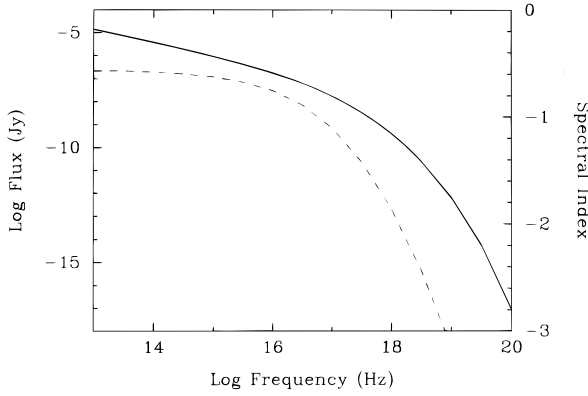


FIG. 4.—Spectrum (solid line) and spectral index (dashed line) of standard age-limited model ($B_1 = 6 \times 10^{-7}$ G, $\eta = 1$, no escape).

The transition in spectral shape as B_1 increases and moves from the age-limited to the loss-limited regime is illustrated in Figure 10. The loss-limited spectra stand out for lesser curvature and for extending to considerably higher X-ray energies. Values of R_{18} and α_{18} for these models are also included in Table 1, and Figures 11 and 12 plot R_{18} and α_{18} versus B_1 (for different gyrofactors).

6.5. Gyrofactor Dependence

For loss-limited models, equation (14) shows that at any given point on the shock surface (i.e., for a particular value of θ_{Bn}), $E_{m1} \propto (\eta R_J)^{-1/2}$. Now $R_J \propto (1 + \eta^2)^{-1}$, so for large η we have $E_{m1} \propto \eta^{1/2}$, and we would expect harder spectra as η increases, other parameters being held constant. While this is true at a given position on the shock, the variation of R_J with θ_{Bn} becomes more strongly peaked around $\theta_{Bn1} = 90^\circ$, and the value at $\theta_{Bn1} = 0$ actually decreases. So the appropriate value of E_{m1} to use to estimate the frequency where the integrated spectrum begins to deviate from a power law is some average over θ_{Bn1} and actually falls slightly with η , for $\eta > 10$. This is shown in Figure 13, with three models with $t = 990$ years and $u_8 = 3.1$, as before, and $B_1 = 1 \times 10^{-5}$ G, with $\eta = 1, 10$, and 50. The integrated fluxes of those three images are 0.31, 0.41, and 0.31 μ Jy, respectively. The narrowing of the zone containing the most energetic particles can easily be seen from Figure 13, and that narrowing counteracts the rise of a factor of 7 in the peak value of E_{m1} , so that the total flux varies only by about 30%.

The spectra show similar shapes, with larger η values dropping the fluxes by a roughly constant factor over almost two decades in frequency. Figure 14 shows spectra for $\eta = 1, 10$, and 50. Little change is apparent. The spectral indices of the models are shown in Figure 15; except at the highest frequencies, where the total flux is very low, all three spectra are quite similar.

For age-limited models, equation (18) shows that for large η , $E_{m2} \propto (\eta R_J)^{-1} \propto \eta$, but the stronger R_J -dependence means that the narrowing of emission around the equator should be even more severe than for loss-limited models. For $B_1 = 6 \times 10^{-7}$ G, Figure 16 shows this. (Actually the $\eta = 50$ case is loss limited at the equator.) The spectra are shown in Figure 17, with spectral indices in Figure 18. The spectra are eventually considerably steeper than for the loss-limited case.

In escape models, η has no effect if E_{m3} is less than either E_{m1} or E_{m2} , since E_{m3} has no η -dependence at all. (There is a slight effect on the detailed shape of external emission, but that has no effect on the integrated spectrum and is almost imperceptible in the halo structure, which is in any case dominated by escaping electrons, which are those diffusing where $\eta = 100$, independent of E_{m3} .)

6.6. Maximum MHD Wavelength Dependence

For escape models, from equation (19) we see that the only important parameter is the product $\lambda_{\max} B_1$. Three spectra are shown in Figure 19, for $B_1 = 3 \times 10^{-6}$ G and $\lambda_{\max} = 10^{16}, 10^{17}$, and 10^{18} cm. (Though the results are independent of η , $\eta = 10$ was used.) The spectra have essentially the same shape and have dropped by a factor of 2.5–4 at the frequency corresponding to each E_{m3} value. Slopes are shown in Figure 20.

6.7. Age Dependence

If shock acceleration of electrons has an overall efficiency that varies in the same sense as the shock velocity, as seems likely, the synchrotron spectrum will have a normalization that will drop with time. However, since a given remnant is typically of unknown age, more important are changes in spectral shape, normalized to the same radio flux. Results in this section have been so normalized. Note that since all the present results are for Sedov-phase dynamics, age and shock velocity can be used interchangeably to describe remnant age, with the relations

$$u_{\text{sh}} = 1.23 \times 10^{10} E_{51}^{1/5} \left(\frac{\mu}{1.4} \right)^{-1/5} n_0^{-1/5} t_{\text{yr}}^{-3/5} \text{ cm s}^{-1} \\ \equiv 7.76 \times 10^9 k^{1/5} t_{\text{yr}}^{-3/5} \text{ cm s}^{-1} \quad (34)$$

or

$$t_{\text{yr}} = 3.03 \times 10^3 u_8^{-5/3} E_{51}^{1/3} \left(\frac{\mu}{1.4} \right)^{-1/3} n_0^{-1/3} \\ \equiv 1.41 \times 10^3 u_8^{-5/3} k^{1/3}. \quad (35)$$

As a remnant ages, it will move from age-limited to loss-limited (unless escape dominates first). In the age-limited phase, equation (17) shows that E_{m2} rises only slowly with time, so the spectrum should only gradually change shape. Figure 21 shows this effect, with spectra at ages of 300, 990, and 10,000 years, for three models with $\eta = 1$ and low upstream magnetic field, $B_1 = 6 \times 10^{-7}$ G. The model at 990 years is in fact that of § 6.1 above. At the first two times, the model is age limited but becomes loss limited at 10,000 years; the X-ray flux can be observed to rise, then fall with time. Figure 22 shows three models that are loss-limited throughout, with a more pronounced drop in the X-ray/radio ratio (i.e., larger R_{18}); equation (14) shows that $E_{m1} \propto u_8 \propto t^{-3/5}$. These models also have ages of 300, 990, and 10,000 years (again, the second is the loss-limited model of § 6.2), and even at the latter age, there is still appreciable X-ray flux at kilo-electron volt energies. Models limited by escape should maintain a constant spectral shape, if λ_{\max} doesn't change, until eventually E_{m1} drops below E_{m3} and they become loss limited. The models in Table 1 show that over a wide range of η , B_1 parameter space, a remnant can

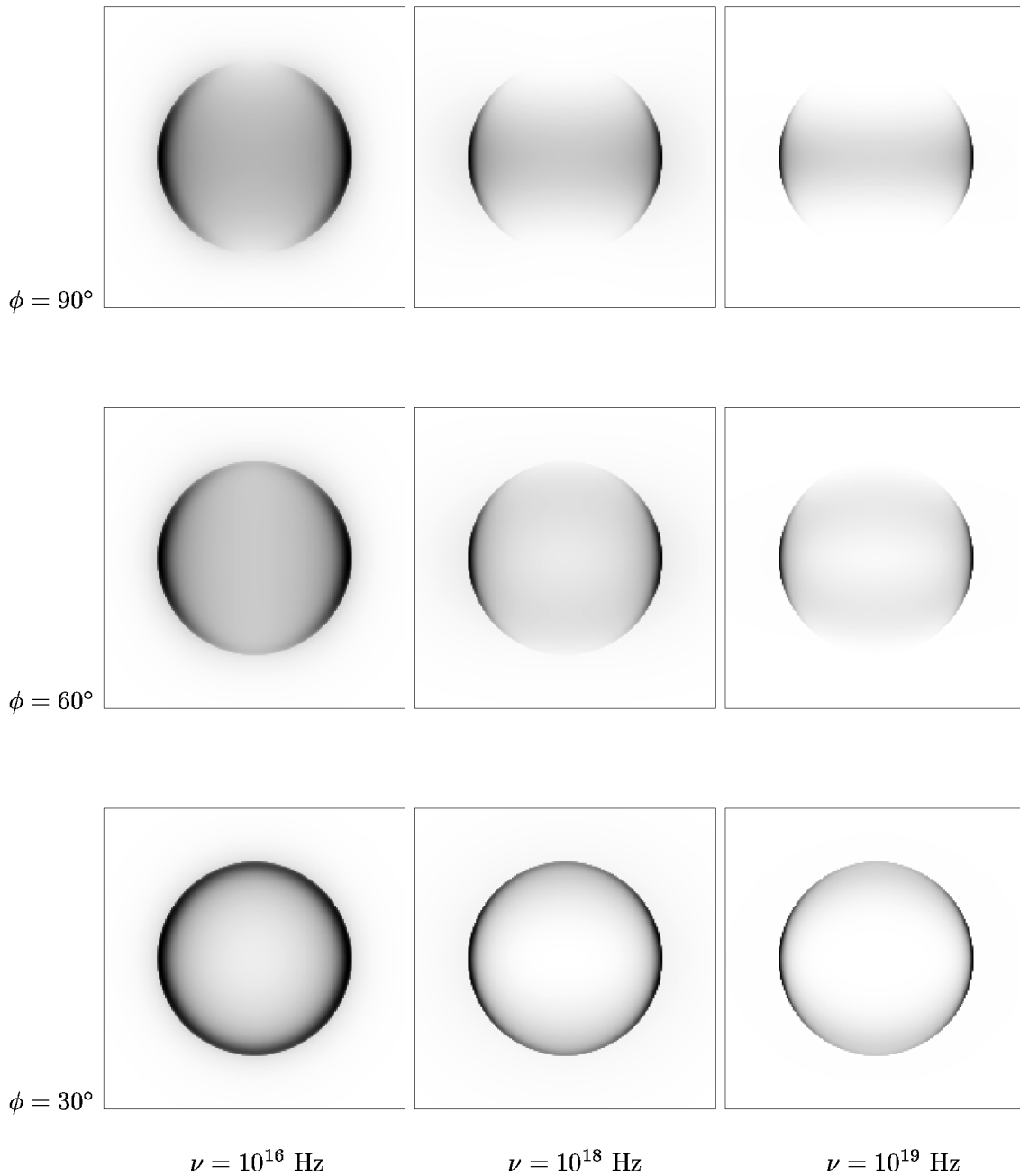


FIG. 5.—Images at several frequencies and aspect angles for the standard age-limited model

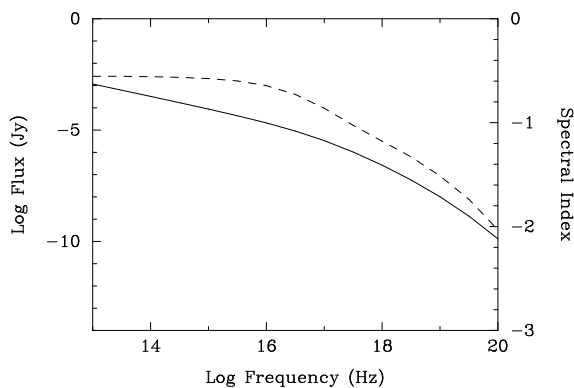


FIG. 6.—Spectrum (solid line) and spectral index (dashed line) of standard loss-limited model ($B_1 = 10^{-5}$ G, $\eta = 10$, no escape).

be expected to fade in 4 keV synchrotron X-rays by about a factor of 10 as it ages from 10^3 to 10^4 years, with a spectral steepening of about 1 in the spectral index near 4 keV.

6.8. Modifications of the Standard Model

The early evolutionary phases of the remnant have been treated in a fairly cavalier fashion here, with the synchrotron emissivity simply truncated interior to the radius of a fluid element that was shocked at the supernova ejection velocity, here taken to be 10^4 km s $^{-1}$. For loss-limited models, the effects of this are small, as should be expected, since electrons currently radiating were accelerated rather recently compared to the age of the remnant, which removes any strong sensitivity to conditions at early times. This weak dependence can be seen from Figures 23 and 24,

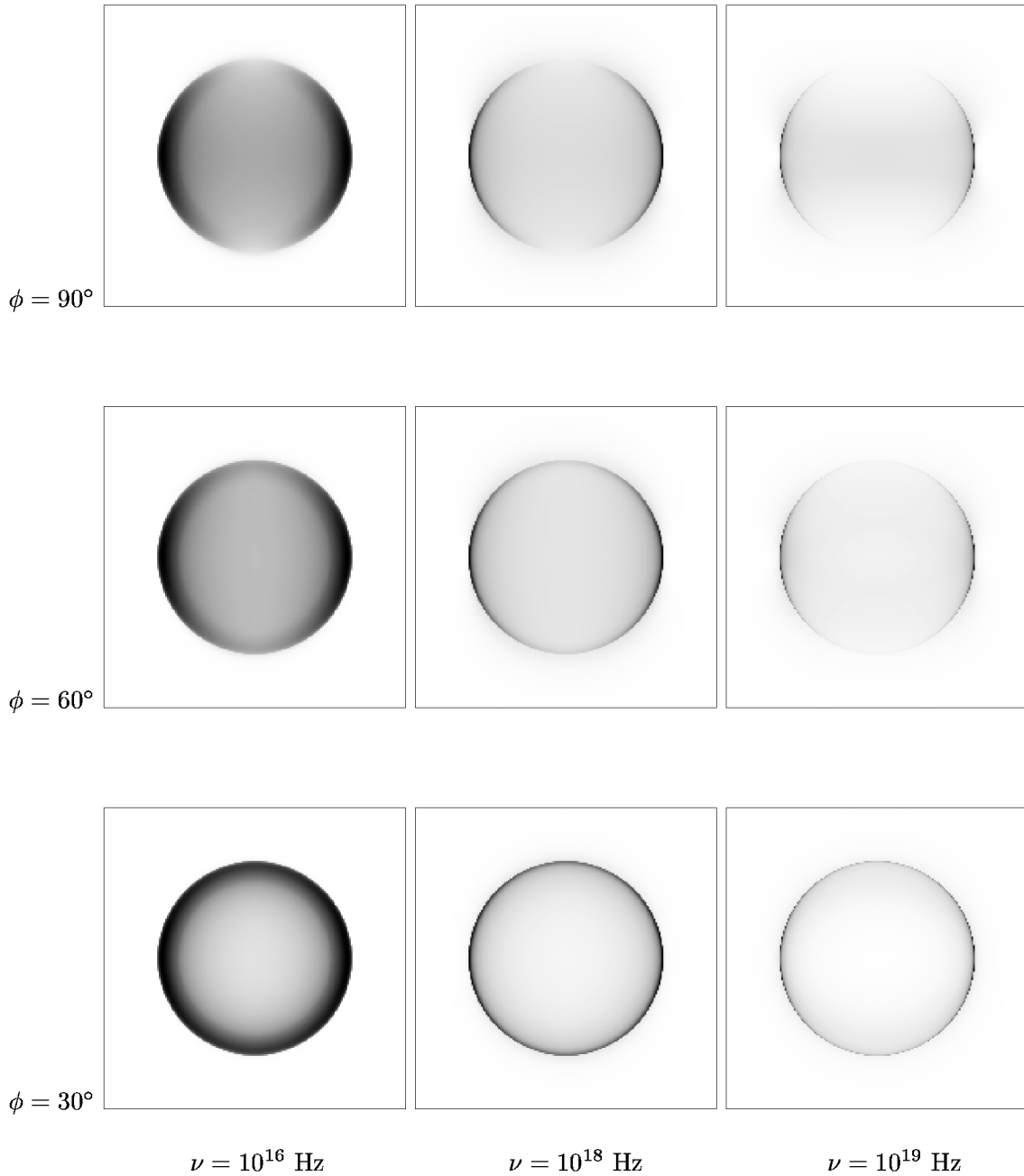
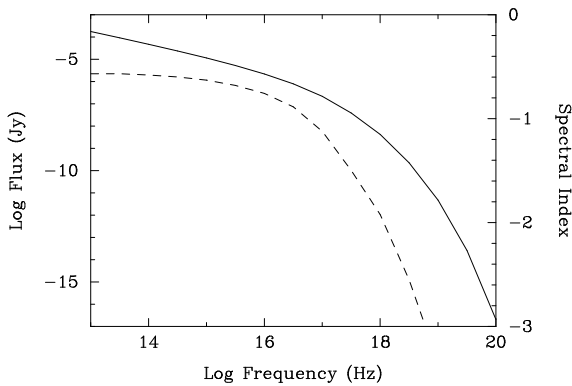


FIG. 7.—Images at several frequencies and aspect angles for the standard loss-limited model

FIG. 8.—Spectrum (solid line) and spectral index (dashed line) of standard escape-limited model ($\lambda_{\text{max}} = 10^{17}$ cm).

which compare models cut off within 10,000 and 20,000 km s⁻¹ in images at 4 keV and spectra. Models have $B_1 = 3 \times 10^{-6}$ G and $\eta = 10$. Images at $\phi = 90^\circ$, 60° , and 30° show small changes in structure near the location corresponding to the cutoff velocity, but those changes make very little difference to the integrated spectrum. A proper treatment of pre-Sedov phases might, however, appear significantly different.

For age-limited models, a higher shock velocity at early times can cause a significant difference, since most electrons currently radiating at the highest energies were in the system at early times. From equation (17), and recalling that $t_{\text{tr}} \propto u_0^{-5/3}$, we have $E_{m0} \propto u_0^{1/3}$. In addition, the smaller value of t_{tr} for larger u_0 will increase the term $1 - (t/t_{\text{tr}})^{-1/5}$, so that E_{m2} can be considerably larger. For a model with

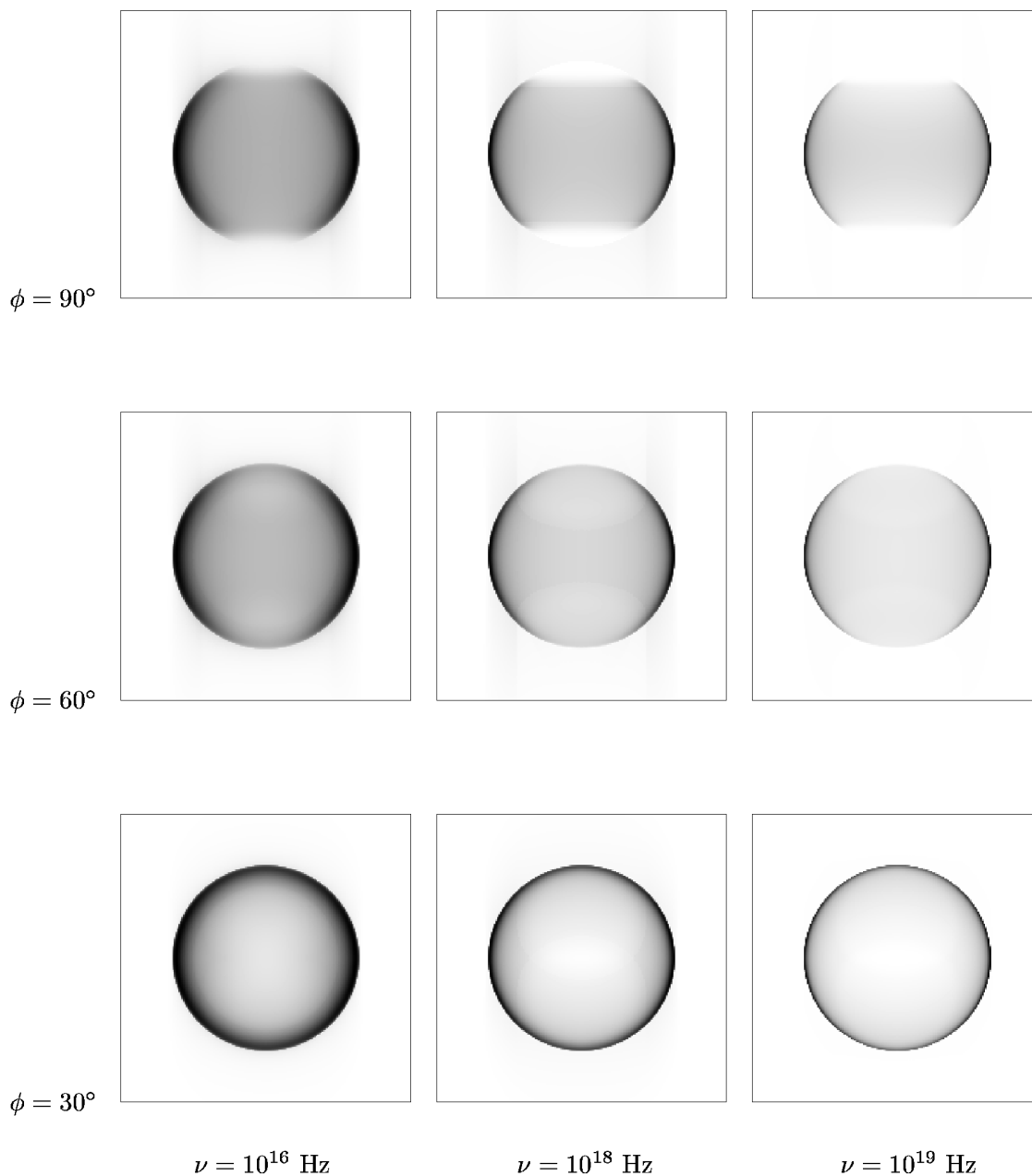


FIG. 9.—Images at several frequencies and aspect angles for the standard escape-limited model

$E_{m1} \sim E_{m2}$, such as the standard age-limited model, this increase causes the spectrum to roll off at a substantially higher frequency and can also push the model into the loss-limited regime, with a considerable effect on the spectrum. The values of R_{18} and α_{18} in Table 1 for several age-limited models illustrate this hardening compared to the standard age-limited model. With small adjustments of the parameters, similar (R_{18}, α_{18}) values can be found for models with different u_0 ; for instance, a model with $\eta = 3$, $B_1 = 0.3 \mu\text{G}$, and $u_0 = 20,000 \text{ km s}^{-1}$ is very similar to the standard age-limited model and can fit the spectrum of SN 1006 equally well.

The variation of electron acceleration efficiency with shock velocity can cause a change in the relative importance of radiation from fluid elements just behind the shock and in the remnant interior. The standard models have assumed

the normalization factor, K , to be constant. Plausible alternatives include assuming the efficiency to be a constant fraction of postshock pressure ($K \propto u_{\text{sh}}^2$) or assuming that a constant fraction of electrons entering the shock are accelerated ($K \propto u_{\text{sh}}$). Figure 25 shows images of these models for $\phi = 90^\circ$, at 10^{18} Hz and for $B_1 = 6 \times 10^{-7} \text{ G}$ and $\eta = 1$.

The profiles of Figure 26 are almost identical and probably impossible to discriminate in view of other physical effects not modeled, such as orientation effects of the magnetic field and the observed radial postshock field in young SNRs. Figure 27 shows that the integrated spectrum is hardly affected as well. Thus the results summarized in Table 1, for dropoffs and spectral indices at 4 keV, should be insensitive to assumptions about variation of K with shock velocity.

We have assumed a fixed value of the low-energy electron

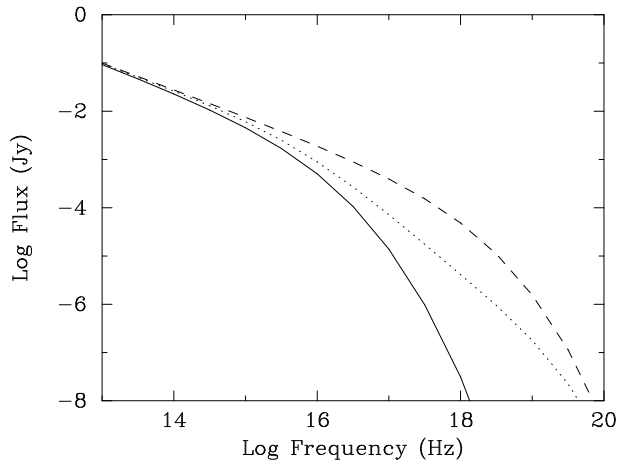


FIG. 10.—Spectra of three models with different values of B_1 , illustrating the transition from age-limited to loss-limited. All have $\eta = 1$; $B_1 = 3 \times 10^{-7}$ G (solid line), $B_1 = 3 \times 10^{-6}$ G (dashed line), and $B_1 = 3 \times 10^{-5}$ G (dotted line).

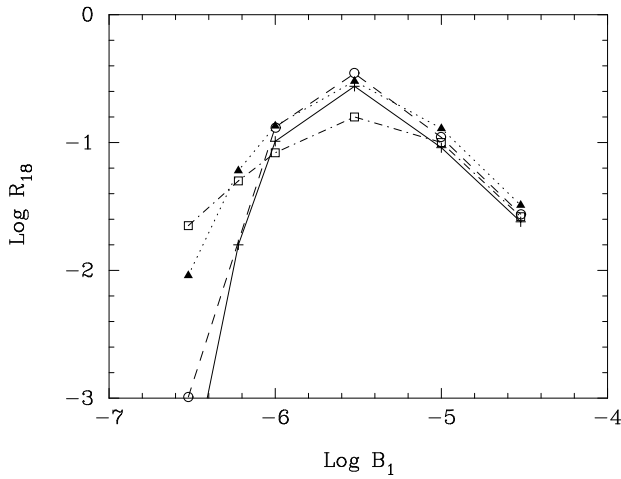


FIG. 11.—Decrement factor, R_{18} (ratio of flux at $\nu = 10^{18}$ Hz to extrapolation from low frequencies), vs. upstream magnetic field, B_1 , for $\eta = 1$ (solid line), $\eta = 3$ (dashed line), $\eta = 10$ (dotted line), and $\eta = 50$ (dot-dashed line).

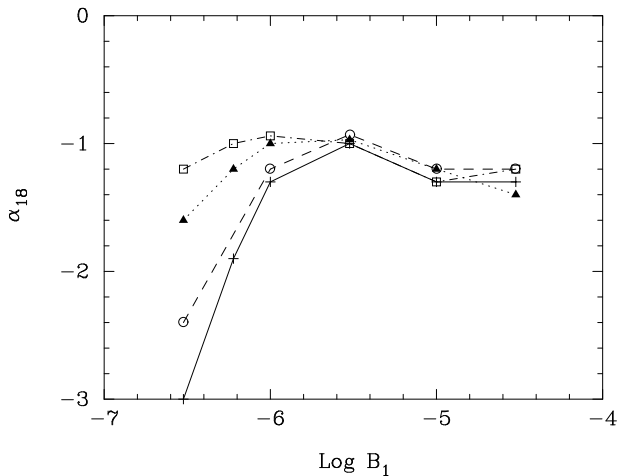


FIG. 12.—Spectral index at 10^{18} Hz, α_{18} , vs. upstream magnetic field strength, B_1 , for $\eta = 1$ (solid line), $\eta = 3$ (dashed line), $\eta = 10$ (dotted line), and $\eta = 50$ (dot-dashed line).

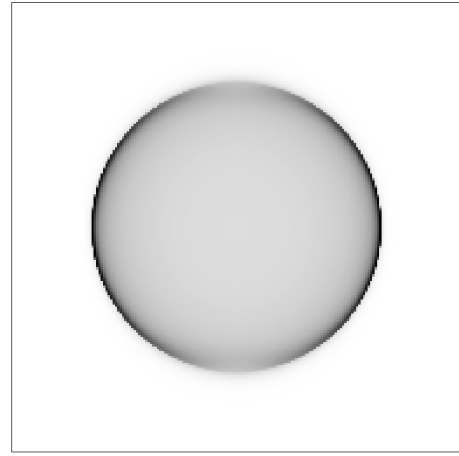


Figure 13(a): $\eta = 1$

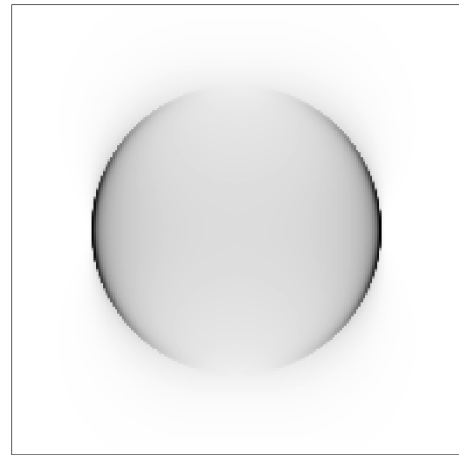


Figure 13(b): $\eta = 10$

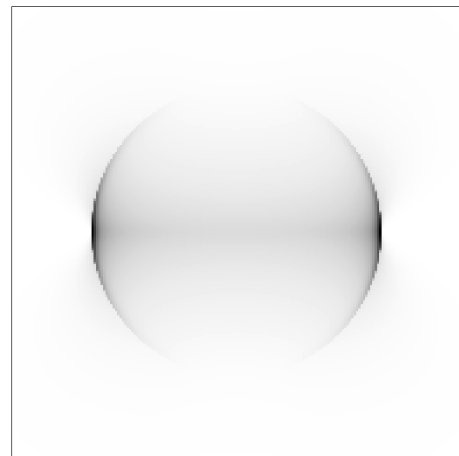


Figure 13(c): $\eta = 50$

FIG. 13.—Images at 10^{18} Hz (aspect angle 90°) of loss-limited models with varying η and $B_1 = 10^{-5}$ G.

spectral index. It might be expected that changing that value, while obviously changing the spectral shape, would have little effect on R_{18} , which is after all measured with respect to the extrapolated low-frequency spectrum. This is in fact the case; models with $s = 1.8$ and $s = 2.4$, but otherwise the same as the standard age-limited (Fig. 4) and loss-limited (Fig. 6) models, were run with the result that $\log R_{18}$

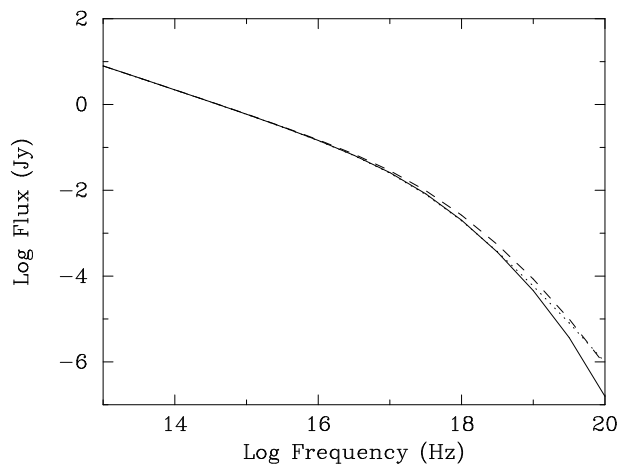


FIG. 14.—Spectra of loss-limited models shown in Fig. 13, for $\eta = 1$ (solid line), $\eta = 10$ (dotted line), and $\eta = 50$ (dashed line).

changed by 0.2 over that range in s (a range of 0.3 in α), while $\alpha_{18} - \alpha$, the increase in spectral slope at 10^{18} Hz over that at radio frequencies, changed by less than 0.1. Thus those observables are robust with respect to the low-frequency spectral index.

7. DISCUSSION

The three mechanisms for producing spectral rolloffs result in two distinct spectral shapes: the age-limited and escape models have rather similar spectra, while the loss-limited models are considerably harder beyond the initial rolloff. Of course, the classification of models by mechanism is imprecise, since each model involves a superposition of spectra with various values of E_m , which vary with position differently, and for substantial volumes of parameter space two competing limiting mechanisms can produce intermediate shapes. Large values of η , coupled with large magnetic field values (extreme loss-limited models), produce spectra that are the least curved over bandpasses of more than 1 order of magnitude.

The escape-limited models are the most homogeneous class. They all have virtually identical spectral shapes that can be characterized completely by a single parameter, the

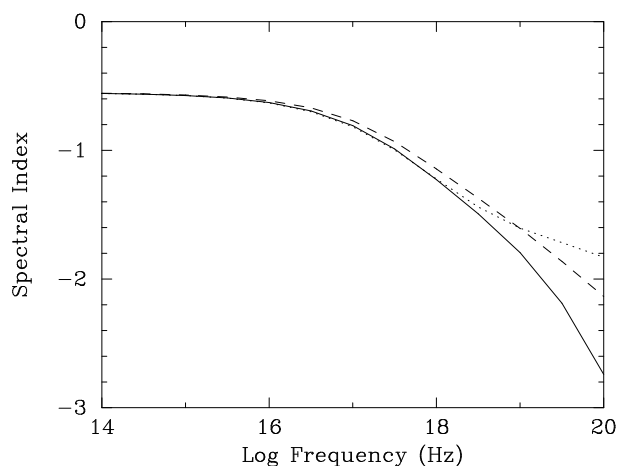


FIG. 15.—Spectral indices of loss-limited spectra shown in Fig. 14, for $\eta = 1$ (solid line), $\eta = 10$ (dotted line), and $\eta = 50$ (dashed line).

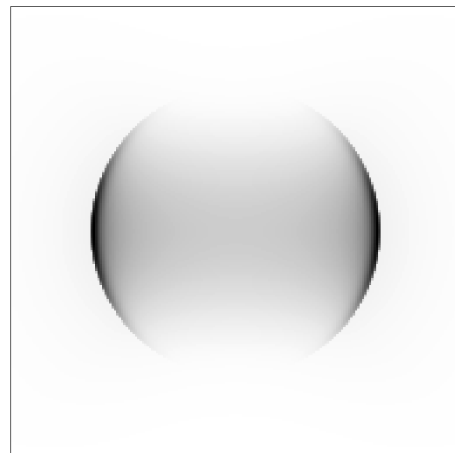


Figure 16(a): $\eta = 1$

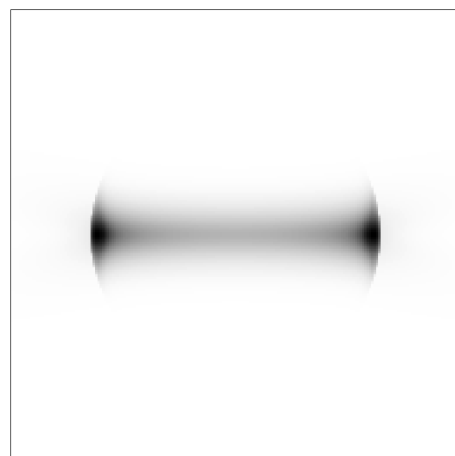


Figure 16(b): $\eta = 10$

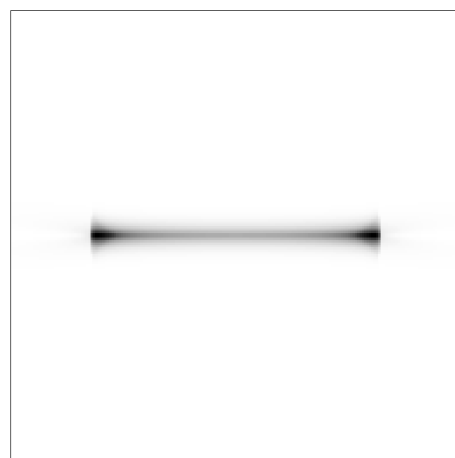


Figure 16(c): $\eta = 50$

FIG. 16.—Images at 10^{18} Hz (aspect angle 90°) of age-limited models with varying η and $B_1 = 6 \times 10^{-7}$ G.

frequency emitted by electrons with energy $E_m(\theta_{Bn} = 90^\circ) \equiv E_{m90}$, calculated from equation (19). At that frequency, $\nu_{m90} \propto B_1 E_{m90}^2 \propto B_1^3 \lambda_{\max}^2$, the spectrum has dropped by about a factor of 2.5 from the low-frequency extrapolation. (However, the highest value of λ_{\max} illustrated in Fig. 19 does not quite follow this scaling, having dropped a factor of 4 at ν_{m90} , since it is only marginally

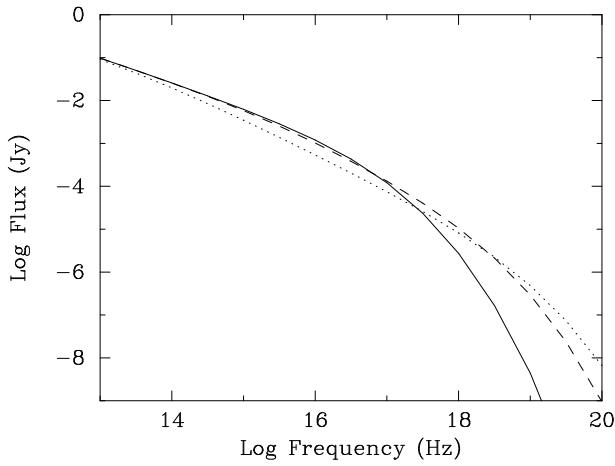


FIG. 17.—Spectra of age-limited models shown in Fig. 16, for $\eta = 1$ (solid line), $\eta = 10$ (dotted line), and $\eta = 50$ (actually now loss limited) (dashed line).

escape limited: E_{m3} is only slightly less than E_{m1} .)

Age-limited models vary the most with η . All are more curved than loss-limited models and slightly less curved than escape-limited models. Thus low magnetic field values,

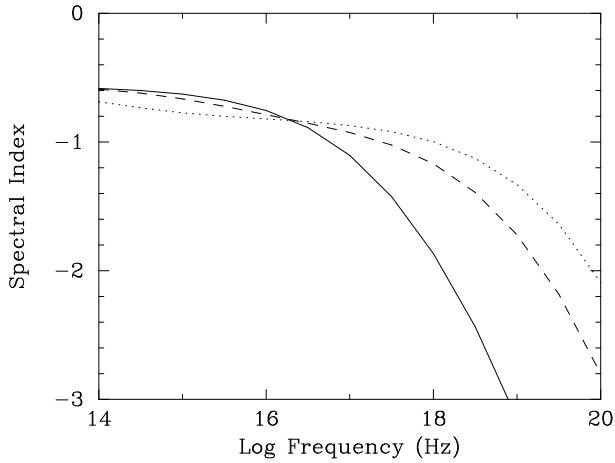


FIG. 18.—Spectral indices of age-limited spectra shown in Fig. 17, for $\eta = 1$ (solid line), $\eta = 10$ (dotted line), and $\eta = 50$ (dashed line).

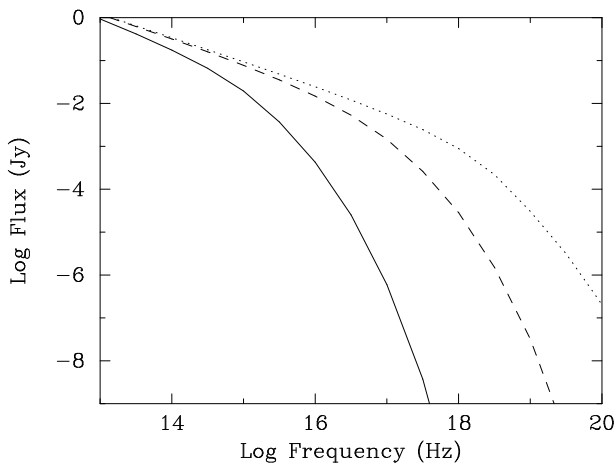


FIG. 19.—Spectra of escape-limited models, for $\lambda_{\max} = 10^{16}$ cm (solid line), $\lambda_{\max} = 10^{17}$ cm (dashed line), and $\lambda_{\max} = 10^{18}$ cm (dotted line).

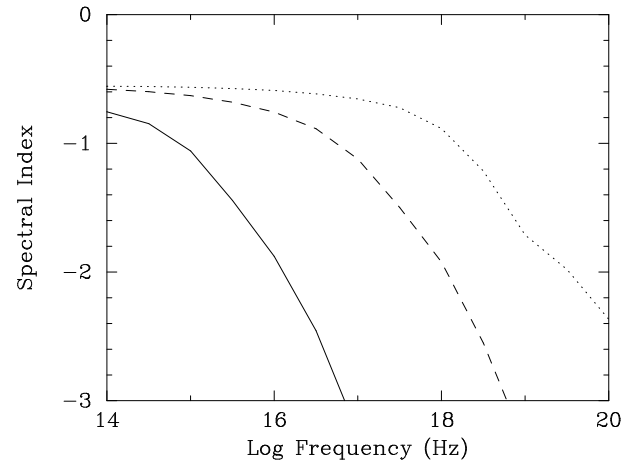


FIG. 20.—Spectral indices of escape-limited spectra shown in Fig. 19, for $\lambda_{\max} = 10^{16}$ cm (solid line), $\lambda_{\max} = 10^{17}$ cm (dashed line), and $\lambda_{\max} = 10^{18}$ cm (dotted line).

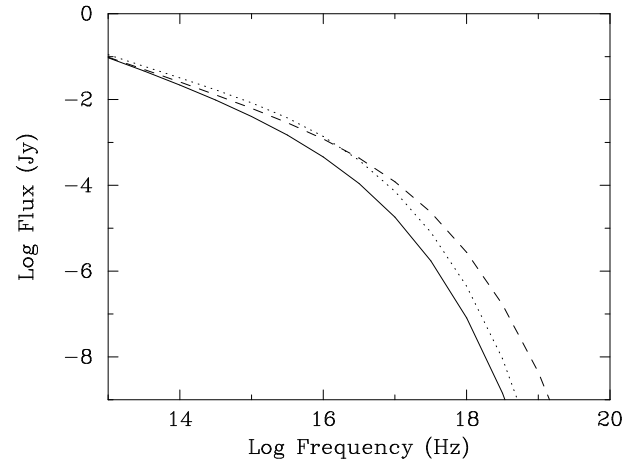


FIG. 21.—Spectra of three age-limited models, at different times. $B_1 = 6 \times 10^{-7}$ G, $\eta = 1$; $t = 300$ years (solid line), $t = 990$ years (dashed line), and $t = 10,000$ years (actually partly loss limited) (dotted line).

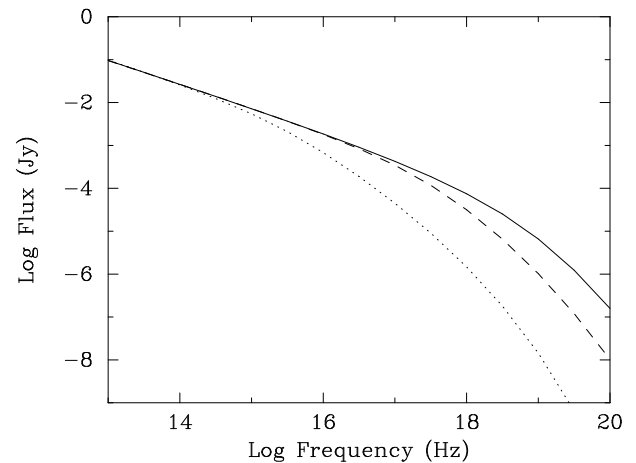


FIG. 22.—Spectra of three loss-limited models, at different times. $B_1 = 10^{-5}$ G, $\eta = 10$; $t = 300$ years (solid line), $t = 990$ years (dashed line), and $t = 10,000$ years (dotted line).

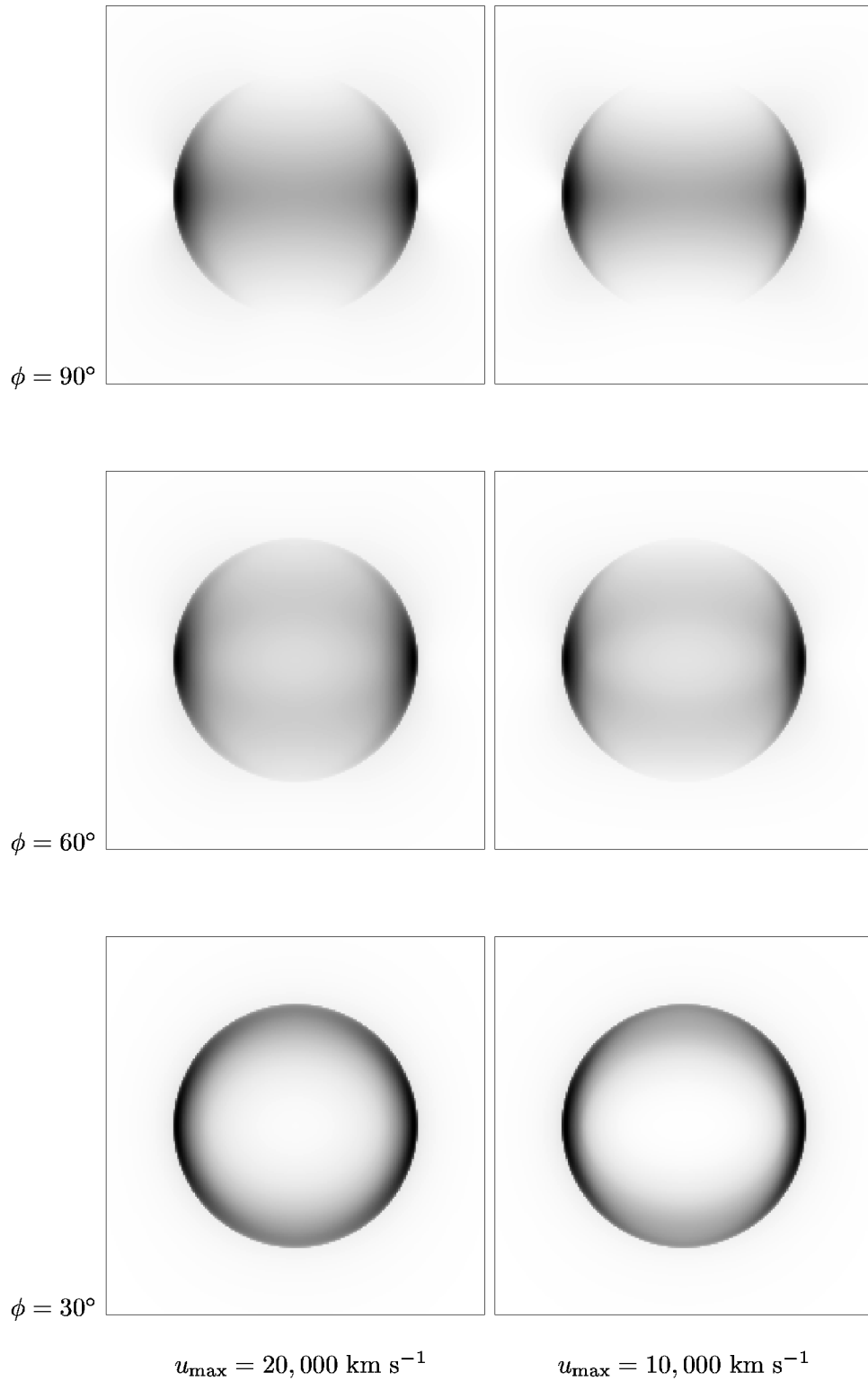


FIG. 23.—Images at three aspect angles of a model with $\eta = 10$ and $B_1 = 3 \times 10^{-6} \text{ G}$, with inner velocity cutoff at 10,000 and 20,000 km s^{-1}

which tend to result in age limitation, give the widest range of spectral shapes. For the age-limited class, as opposed to the escape-limited class, the quantity $v_{m90}(B_1, \eta)$ does not correspond to a constant decrement. For $\eta = 1$, the spectrum at v_{m90} has dropped below the low-frequency extrapolation by a factor of 5–6 as B_1 rises from 0.3 to 1 μG . The corresponding values for $B_1 = 0.3 \mu\text{G}$, as η goes from 1 to

10, are from 5 to 24; the spectrum changes shape substantially for $\eta = 10$.

Loss-limited models, for high magnetic field values ($B_1 > 10 \mu\text{G}$) and/or high gyrofactors ($\eta > 10$), can produce extended, almost straight spectral regions above the initial steepening, as the drastic constriction of emission around the remnant equator is partially balanced by more rapid

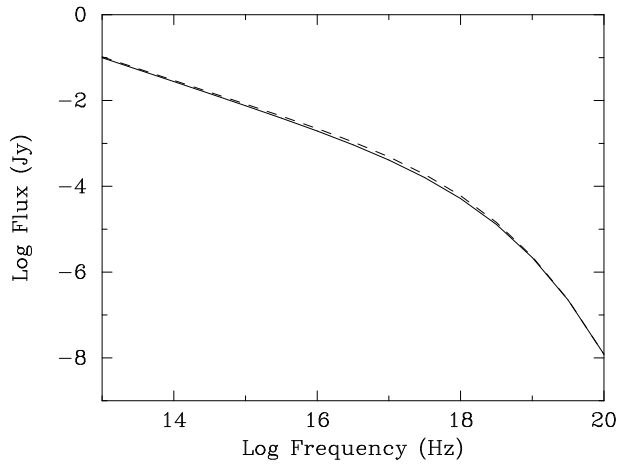


FIG. 24.—Spectra of models of Fig. 23, with cutoff interior to 10,000 km s⁻¹ (solid line) and cutoff interior to 20,000 km s⁻¹ (dashed line).

acceleration there. Realistic remnants expanding into inhomogeneous external material may not be able to realize this effect to the extent shown by the idealized models.

For both age- and loss-limited models, the dependence of the crude spectral descriptors R_{18} and α_{18} on η is far less than predicted by simply examining $E_{m90}(\eta R_i)$ because of the effect of different θ_{Bn} -dependence shown dramatically in Figures 13 and 16. Loss- and age-limited models show very little variation with η , while, as mentioned above, escape-limited models have absolutely no variation with η . Thus for observable effects in the range of a few kilo-electron volts, gyrofactor dependences are likely to be unimportant. (If we had chosen a much higher fiducial energy, the η -dependence would be stronger and in the expected direction, as is apparent from Figs. 14 and 17.)

Again within each class, dependence on remnant age affects models primarily through the shock velocity, u_8 , that is, on the combination $(E/n_0)^{1/5} t^{-3/5}$. Models of different ages, if belonging to the same class, have similar spectral shapes, with $v(E_{m90})$ for each corresponding to a fairly similar dropoff factor as given by the scaling of E_{m90} with u_8 . For age-limited models, $E_{m2} \propto [1 - (t_u/t)^{0.2}]$, varying by a factor of 2.3 between 300 and 990 years, so $v_{m90} \propto E_{m2}^2$ rises by about 5. The decrement factor at that frequency ranges from 24 at an age of 300 years to 30 at 990 years. For loss-limited models, $E_{m1} \propto u_8 \propto (n_0 t^3)^{-1/5}$, so $v_{m90} \propto t^{-6/5}$. The decrement factor at that frequency varies a bit more, from 20 at 300 years to 40 at 10⁴ years. Still, there is less variation with age within each class than between classes.

The application of these results to individual SNRs then requires considering the three classes of models separately. If the escape mechanism operates, fitting an observed remnant or using its thermal X-rays for an upper limit immediately results in a value of, or limit for, $v_{m3} \propto B_1^3 \lambda_{\max}^2$, with no dependence on η , age, or anything else. Until far better X-ray spectral data on SNRs are available, this possibility will always exist. However, the escape models predict considerably more X-ray emission external to the shock than the others; sensitive imaging observations may be able to indicate whether the escape mechanism is operating or not.

Of the other two mechanisms, age-limited models eventually cross over to become loss limited. The time of this crossover, t_{eq} (eq. [32]), depends on external density as $n_0^{2/9}$,

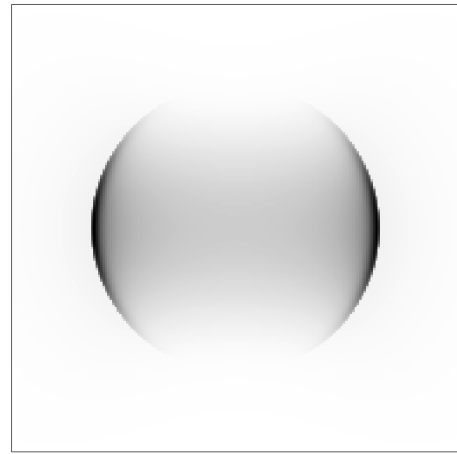


Figure 25(a): $K = \text{const.}$

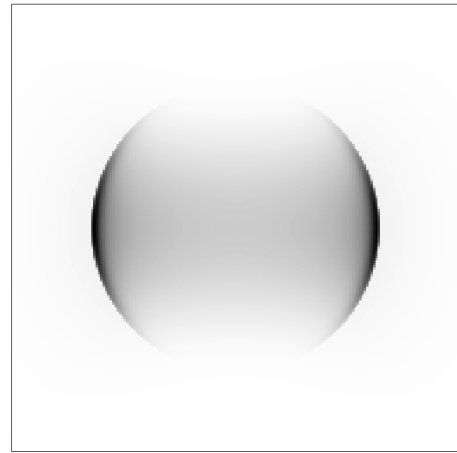


Figure 25(b): $K \propto u_{sh}$

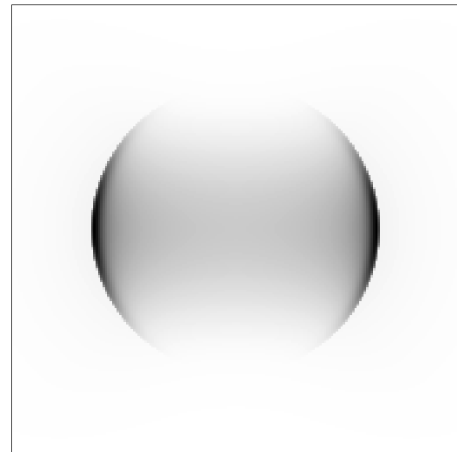


Figure 25(c): $K \propto u_{sh}^2$

FIG. 25.—Images of a model with $\eta = 10$ and $B_1 = 3 \times 10^{-6}$ G but with variant versions of the shock-velocity dependence of the coefficient K of the accelerated electron spectrum.

so that the higher the density, the longer a given remnant will be age limited, though the dependence is fairly weak. During that time, the spectral turnover is governed by $E_{m2} \propto n_0^{-1/3}$, roughly independent of time. For loss-limited models, $E_{m1} \propto (n_0 t^3)^{-1/5}$, so that models with the same value of $n_0 t^3$ will have fairly similar spectra. Thus when

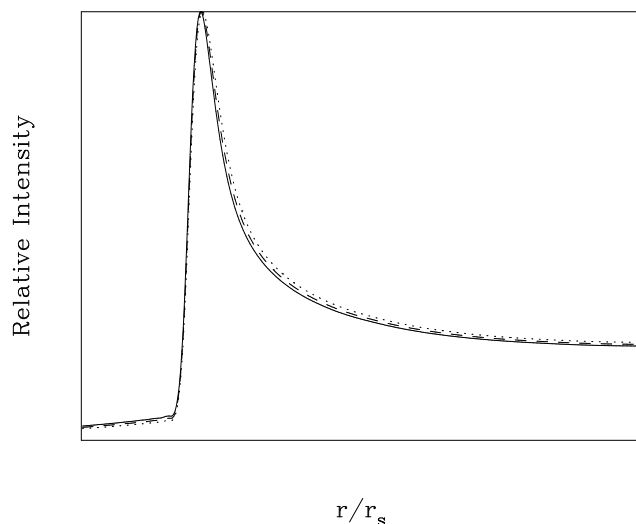


FIG. 26.—Profiles of images of Fig. 25, at a position angle of 90° (horizontal).

$t > t_{\text{eq}}$, higher densities result in somewhat more rapid spectral evolution; the same values of R_{18} and α_{18} will apply at earlier times. This may help account for the lack of conspicuous nonthermal emission from young to middle-aged remnants, with typical upstream densities typically inferred to be near 1, as opposed to the much lower density upstream for SN 1006.

Figure 28 shows the location of models in the (R_{18}, α_{18}) plane, for an age of 990 years; Figure 29 shows many of the same models at an age of 10,000 years. The small differences with η as measured by R_{18} and α_{18} are apparent as the three tracks of models with $\eta = 1, 10$, and 50 are quite close together compared to the separation of models with different B_1 . As models age, they all evolve to the lower right (steeper spectra and fainter fluxes) as is apparent from comparing Figures 28 and 29.

The curves in Figures 28 and 29 are independent of the overall electron acceleration efficiency and of other normalizing parameters, such as the distance, since R_{18} is a relative measure with respect to the radio flux. For the same reason, they also depend on the magnetic field strength far less sensitively than does the total flux density at 4 keV. As

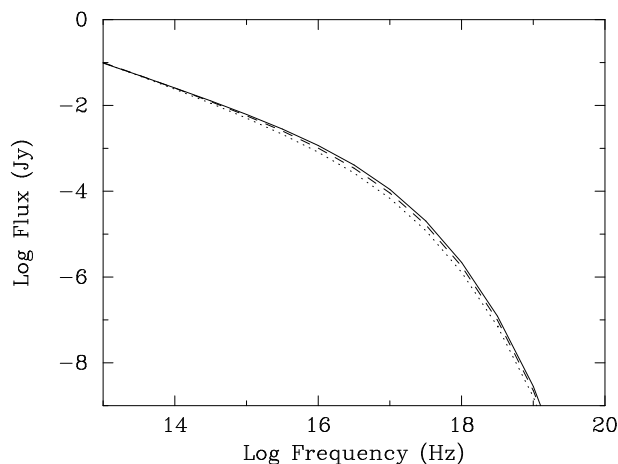


FIG. 27.—Spectra of models of Fig. 25 for $K = \text{constant}$ (solid line), $K \propto u_{\text{sh}}$ (dashed line), and $K \propto u_{\text{sh}}^2$ (dotted line).

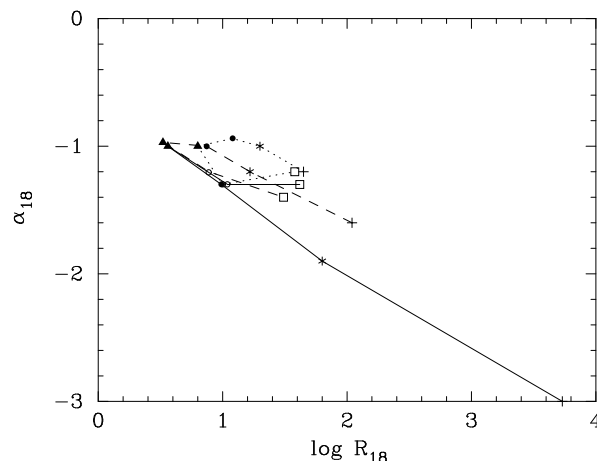


FIG. 28.— R_{18} – α_{18} parameter space for models, at age 990 years for $\eta = 1$ (solid line), $\eta = 10$ (dashed line), and $\eta = 50$ (dotted line). Symbols indicate magnetic field values of $B_1 = 0.3 \mu\text{G}$ (plus signs), $0.6 \mu\text{G}$ (stars), $1 \mu\text{G}$ (filled circles), $3 \mu\text{G}$ (filled triangles), $10 \mu\text{G}$ (open circle), and $30 \mu\text{G}$ (squares).

discussed above, these relative parameters are also insensitive to radio spectral index or electron index, s .

Observed nonthermal X-ray emission from a SNR can then be plotted on Figure 28 to select possible consistent models. In the much more common case of observed thermal emission, one has no information on α_{18} and an upper limit on R_{18} , which may still result in useful conclusions about the age and/or density of a given SNR (bearing in mind that escape models may also be consistent with observations).

It is worthwhile to reiterate the crucial assumptions behind the models of Table 1 and Figures 28 and 29. Sedov dynamics are assumed, the upstream magnetic field and density are assumed uniform, the shock is assumed to have a reasonably well-defined obliquity everywhere on the periphery, no magnetic field amplification (beyond compression) is presumed to occur behind the shock, and the relativistic electrons are presumed not to diffuse substantially behind the shock but are convected with the thermal fluid. Sedov dynamics should be a reasonable

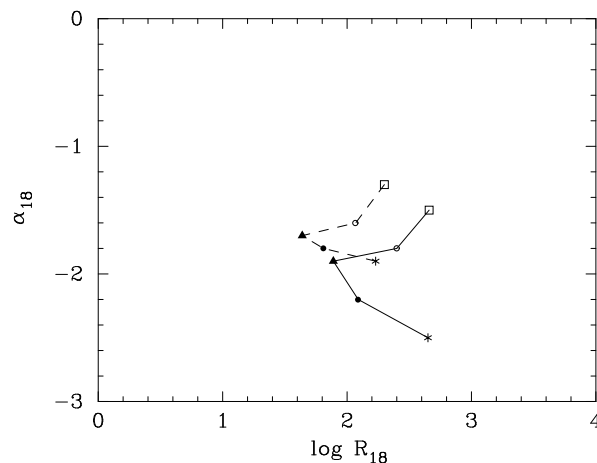


FIG. 29.— R_{18} – α_{18} parameter space for models, at age 10,000 years, for $\eta = 1$ (solid line) and $\eta = 10$ (dashed line). The symbols have the same meanings as in the previous figure.

approximation for all but the young historical remnants, where it is possible that a better description using, say, Chevalier's (1982) self-similar driven wave dynamics should be used. The assumption of constant upstream density and magnetic field strength limits the application of the results either to remnants of Type Ia supernovae, expanding into more or less uniform ISM from an early age, or to older core-collapse remnants that have expanded beyond the bounds of their original stellar-wind bubbles. At earlier times, these remnants may be encountering r^{-2} density profiles and magnetic field strengths falling as r^{-1} with primarily tangential orientation ($\theta_{Bn} \sim 90^\circ$ over most of the periphery); this will have major consequences for the η -dependence of models. If the postshock magnetic field is highly turbulently amplified, the energy evolution of postshock electrons will be modified, and the images will be quite different, though integrated spectral effects may be less. If postshock electrons can diffuse freely (outside the presumably highly turbulent immediate postshock region in which particles are still accelerated), the distribution of internal emission will be quite different, but again the spectra should not show enormous differences from those calculated here.

Finally, it should be stressed that electrons accelerated to these energies can produce detectable teravolt γ -rays through inverse Compton scattering on microwave background photons (Mastichiadis 1996; Pohl 1996; Mastichiadis & de Jager 1996). In particular, Mastichiadis & de Jager (1996) modeled synchrotron X-rays in SN 1006 and made a definite prediction for the expected teravolt flux, which has recently been confirmed with the detection of teravolt γ -rays from SN 1006 by the Collaboration of Australia and Nippon for a Gamma-Ray Observatory in the Outback (CANGAROO) (Tanimori 1997). Work is under way (Baring et al. 1997) to use these results to make predictions of IC γ -rays in general and to combine them with nonlinear numerical simulations of proton acceleration in the shock to derive a total γ -ray spectrum including π^0 -decay γ -rays from cosmic-ray proton collisions with thermal gas and bremsstrahlung γ -rays from electrons.

8. CONCLUSIONS

The basic conclusion of this work is that supernova-remnant blast waves should easily accelerate electrons to X-ray emitting energies, in a way fairly insensitive to details, so that, under a wide range of conditions, the X-ray flux at 4 keV is between 3 and 100 times below the extrapolation from radio wavelengths. Thus nonthermal X-ray emission should be common among SNRs. In most cases, however, observed SNR X-ray emission appears predominantly

thermal. This work shows that a given remnant will produce the maximum nonthermal X-ray emission relative to its radio flux, when its age is roughly comparable to the loss time for electrons in the postshock magnetic field. The remnant of SN 1006 is just at this stage, which explains why it and no other historical remnant has an X-ray spectrum dominated by synchrotron radiation. However, equation (33) shows that for typical interstellar magnetic field strengths, other remnants of a few hundred to a few thousand years of age should still be near enough to that situation ($E_{m1} \sim E_{m2}$) that their nonthermal X-rays may be distinguishable, especially at higher X-ray energies. Even for remnants dominated by thermal emission, that emission is an upper limit for nonthermal X-rays, and the parameter space of upstream magnetic field strength, gyrofactor, and cutoff MHD wavelength can be restricted.

A useful caveat demonstrated in § 5, and worth emphasizing again, is that if one wishes to calculate the spectrum accurately well above a "cutoff" energy, one must perform the full integration of the electron spectral distribution over the single-electron synchrotron emissivity.

All models predict some emission exterior to the shock, though at low surface brightness levels. The detection of this emission should allow immediate inferences about the pre-shock electron diffusion coefficient and may allow discrimination among the three classes of models. In addition, very few models show any curvature in the spectrum before the ultraviolet, so a strong prediction is made for the presence of (faint!) nonthermal optical emission from SNRs in general. This emission should be extremely well correlated with the radio emission, so optical searches can concentrate on radio-bright regions.

If nonthermal X-ray emission does not turn out to be common among supernova remnants, substantial modifications in some of our basic ideas about shock acceleration may be required. Escape models can always be invoked, but they have the unpleasant side effect of constraining high-energy proton acceleration as well, with serious consequences for our ideas about the origin of Galactic cosmic rays. A search for nonthermal components in SNR X-ray emission above a few kilo-electron volts, where thermal components should be disappearing, should be a high priority for future X-ray missions such as *AXAF*, *XMM*, and *ASTRO-E*.

It is a pleasure to acknowledge extensive discussions with D. Ellison and R. Jokipii over several years, as well as particular discussions with O. de Jager and T. Gaisser. This work was supported by NASA through grants NAG 5-2212 and NAG 5-2844.

REFERENCES

- Achterberg, A., Blandford, R. D., & Reynolds, S. P. 1994, *A&A*, 281, 220 (ABR)
 Ammosov, A. E., Ksenofontov, L. T., Nikolaev, V. S., & Petukov, S. I. 1994, *Astron. Lett.*, 20, 157
 Baring, M. G., Ellison, D. C., Reynolds, S. P., Grenier, I., & Goret, P. 1998, in preparation
 Becker, R. H., Szymkowiak, A. E., Boldt, A. E., Holt, S. S., & Serlemitsos, P. J. 1980, *ApJ*, 240, L33
 Bell, A. R. 1978, *MNRAS*, 182, 147
 Blandford, R. D., & Eichler, D. 1987, *Phys. Rep.*, 154, 1
 Chevalier, R. A. 1982, *ApJ*, 258, 790
 Draine, B. T., & McKee, C. F. 1993, *ARA&A*, 31, 373
 Drury, L. O'C. 1983, *Rep. Prog. Phys.*, 46, 973
 ———, 1991, *MNRAS*, 251, 340
 Duin, R. M., & Strom, R. G. 1975, *A&A*, 39, 33
 Ellison, D. C., Baring, M. G., & Jones, F. C. 1995, *ApJ*, 453, 873
 Ellison, D. C., Jones, F. C., & Reynolds, S. P. 1990, *ApJ*, 360, 702
 Ellison, D. C., & Reynolds, S. P. 1991, *ApJ*, 382, 242
 Esposito, J. A., Hunter, S. D., Kanbach, G., & Sreekumar, P. 1996, *ApJ*, 461, 820
 Forman, M. A., & Drury, L. O'C. 1983, *Proc. 18th Int. Cosmic-Ray Conf. (Bangalore)*, 2, 267
 Forman, M. A., & Morfill, G. 1979, *Proc. 16th Int. Cosmic-Ray Conf.*, 3, 467
 Gaisser, T. K. 1994, *Cosmic Rays and Particle Physics* (Cambridge: Cambridge Univ. Press)
 Gaisser, T. K., Protheroe, R. J., & Stanev, T. 1998, *ApJ*, 492, 227
 Giacalone, J., Burgess, D., Schwartz, S., & Ellison, D. C. 1992, *Geophys. Res. Lett.*, 19, 433
 Green, D. A. 1991, *PASP*, 103, 209
 Jokipii, J. R. 1987, *ApJ*, 313, 842
 Lagage, P. O., & Cesarsky, C. J. 1983, *A&A*, 118, 223

- Mastichiadis, A. 1996, *A&A*, 305, L53
Mastichiadis, A., & de Jager, O. C. 1996, *A&A*, 311, L5
Pacholczyk, A. G. 1970, *Radio Astrophysics* (San Francisco: Freeman)
Pohl, M. 1996, *A&A*, 307, 57
Reynolds, S. P. 1992, in *Particle Acceleration in Cosmic Plasmas*, ed. G. P. Zank & T. K. Gaisser (New York: American Institute of Physics), 409
———. 1994, *ApJS*, 90, 845
———. 1995, *Proc. 24th Int. Cosmic-Ray Conf. (Rome)*, 2, 17
———. 1996, *ApJ*, 459, L13 (Paper I)
Reynolds, S. P., & Chevalier, R. A. 1981, *ApJ*, 245, 912
Reynolds, S. P., & Hornschemeier, A. E. 1996, in *Röntgenstrahlung from the Universe*, ed. H. U. Zimmermann, J. E. Trümper, & H. Yorke (Garching: MPI), 271
Reynolds, S. P., & Ellison, D. C. 1992, *ApJ*, 399, L75
Reynolds, S. P., & Gilmore, D. A. 1993, *AJ*, 106, 272
Tanimori, X. 1997, *IAU Circ.* 6706
Toor, A. 1980, *A&A*, 85, 184
Webb, G. M., Drury, L. O'C., & Biermann, P. L. 1984, *A&A*, 137, 185